Natural poloidal asymmetry and neoclassical transport of impurities in tokamak plasmas

Patrick Maget, Judith Frank, Timothée Nicolas, Olivier Agullo, Xavier Garbet, Hinrich Lütjens

To cite this version:

Patrick Maget, Judith Frank, Timothée Nicolas, Olivier Agullo, Xavier Garbet, et al.. Natural poloidal asymmetry and neoclassical transport of impurities in tokamak plasmas. Plasma Physics and Controlled Fusion, 2020, 62 (2), pp.025001. 10.1088/1361-6587/ab53ab . hal-02401330

HAL Id: hal-02401330
https://hal.science/hal-02401330

Submitted on 3 Feb 2020

Natural poloidal asymmetry and neoclassical transport of impurities in tokamak plasmas

Patrick Maget[1], **Judith Frank**[2,1], **Timothée Nicolas**[3], **Olivier Agullo**[2], **Xavier Garbet**[1], **Hinrich Lütjens**[3]

[1] CEA, IRFM, F-13108 Saint Paul-lez-Durance, France.

[2] Aix-Marseille Université, CNRS, PIIM UMR 7345, 13397 Marseille Cedex 20, France.

[3] Centre de Physique Théorique, CNRS, Ecole Polytechnique, Institut Polytechnique de Paris, Route de Saclay, 91128 PALAISEAU

E-mail: `patrick.maget@cea.fr`

Abstract. The neoclassical transport of impurities is investigated for a plasma without toroidal rotation nor anisotropic ion temperature. It is shown that a natural poloidal asymmetry of the impurity density exists in this case, and that it can be described with a simple analytical model. The poloidal asymmetry tends naturally to cancel as the impurity profile evolves towards its steady state, so that the main effect of the poloidal asymmetry is to slow down the impurity flux compared to its predicted value without poloidal asymmetry. The contribution of the asymmetries of the electrostatic potential and of the main ion density can be included in the analytical derivation, thus forming a self-consistent description of the neoclassical impurity flux together with its poloidal distribution. Numerical simulations with a non linear fluid code confirm the analytical findings, showing that the neoclassical transport of impurities is strongly modified by its natural poloidal distribution.

Submitted to: *Plasma Physics and Controlled Fusion*

1. Introduction

The operational space of a fusion reactor results from the balance between the heat source produced by alpha particles and additional heating systems on the one side, and the heat losses produced by the radiation emitted by ions. The inevitable presence of impurities in a fusion plasma greatly enhances the radiative losses and has motivated numerous studies, both experimental and theoretical. The outcome of these works is that impurity transport across magnetic flux surfaces is strongly influenced by collisional (or neoclassical) transport, in particular when the electric charge of the impurity is high. Although it will not be discussed in this paper, it has to be noted that turbulence also plays a key role in the radial transport of impurities, with diffusive and convective components that compete with the neoclassical contribution and often overcome it, as evidenced in numerical [1, 2, 3, 4] or experimental works [5, 6, 7, 8, 9, 10, 11]. To leading order, the main players in the neoclassical impurity transport are the density profile of the main ion, which drives an inward impurity flux that contaminates the plasma core, the main ion temperature profile, that drives a protective outward flux and leads to the concept of temperature screening, and the poloidal asymmetry of the impurity density. The latter effect alters the previous contributions in a complex manner, leading to a large increase or damping of the impurity flux, or even its reversal. The dependence of the flux on these asymmetries can be expressed as a function of the horizontal asymmetry (between the high field side and the low field side) and the vertical asymmetry [12]. Several conditions are known to induce a high level of these asymmetries, such as toroidal rotation [13, 14, 15] or temperature anisotropy [16, 17], and the impurity screening or accumulation that are predicted in these cases are consistent with experimental observations [18, 19]. But the impurity distribution is already asymmetric in more quiet conditions, i.e. without toroidal rotation nor ion temperature anisotropy, and this natural asymmetry can already lead to a significant modification of the radial flux.

We investigate in the present work these natural impurity flux and poloidal distribution arising from neoclassical transport from both analytical and numerical perspectives. Analytical theory shows that the horizontal and vertical impurity asymmetries are strongly related and move along a circle when the collisionality is modified, the center and radius of the circle being set by the density and temperature gradients and the angular position by collisionality, as described in sections 2 and Appendix A. If the electrostatic potential is poloidally symmetric, which is the case to leading order in the context that is considered (no toroidal rotation, isotropic ion temperature), the poloidal asymmetry is evolving toward a uniform poloidal distribution of the impurity. When the electrostatic potential and the ion density have a small poloidal asymmetry, the asymmetry of the impurity can still be determined analytically, but the steady state distribution has a remaining asymmetry. Numerical simulations are performed with the nonlinear MHD code XTOR [20] where neoclassical physics [21], as well as impurity dynamics [22, 23] are implemented. The description of the model is given in section 3 and complemented in the Appendix B. The main result reported in section 4 is that if we start from a flat initial impurity profile, a natural poloidal asymmetry will arise and strongly damp the radial impurity flux, the neoclassical drive being directed inward (when the ion density profile is peaked) or outward (when it is flat). The flux and poloidal distribution are in good agreement with theory predictions, and the slow impurity evolution is consistent with a poloidal asymmetry that decays to zero. The implications for the experimental analysis and for the combined study of impurity transport with MHD activity are discussed in the conclusion (section 5).

2. Impurity flux and its poloidal distribution

2.1. Impurity flux

The neoclassical impurity flux results from the collisional friction between the impurity and the main ion. To leading order, its amplitude is modulated by the poloidal asymmetry of the impurity density itself. But the asymmetry of the main ion density induces corrections that cannot be completely neglected even in the absence of toroidal rotation or temperature anisotropy, as will be shown in the numerical application. A derivation that takes into account both effects is therefore also presented, and extends the domain of applicability of the analytical model. Note that throughout the text the main ion will be referred with the indice "i" while the impurity will be denoted with "a".

2.1.1. Impurity flux for a poloidally symmetric main ion density In the hypothesis where the ion density is a flux function, the flux of an impurity "a" can be expressed in the following form (see Appendix A):

$$\langle \Gamma_a \cdot \nabla\psi\rangle = m_a \nu_a \frac{F^2 T_a \langle n_a\rangle}{e_a^2 \langle B^2\rangle}\left[\left(\frac{1}{\left\langle \frac{b^2}{n}\right\rangle} - \left\langle \frac{n}{b^2}\right\rangle\right)\mathcal{G} + \left(\frac{1}{\left\langle \frac{b^2}{n}\right\rangle} - 1\right)\mathcal{U}\right] \tag{1}$$

where we have defined $F \equiv RB_\varphi$ and

$$\mathcal{G} \equiv \partial_\psi \ln p_a - \frac{T_i}{T_a}\frac{e_a}{e_i}\partial_\psi \ln p_i + C_0^a \frac{T_i}{T_a}\frac{e_a}{e_i}\partial_\psi \ln T_i \tag{2}$$

$$\mathcal{U} \equiv u(\psi)\frac{\langle B^2\rangle}{F}\frac{e_a}{T_a} \tag{3}$$

and

$$u(\psi) = \frac{\mathbf{V_i}\cdot\nabla\theta}{\mathbf{B}\cdot\nabla\theta} - \frac{C_0^a}{\langle B^2\rangle}\left(\left\langle u_{2\parallel i}\right\rangle + F\frac{\partial_\psi T_i}{e_i}\right) \tag{4}$$

$$C_0^a = \frac{3}{2}\frac{1}{1+\frac{T_a}{T_i}\frac{m_i}{m_a}} \tag{5}$$

with $\mathbf{V_i}$ the fluid velocity of the main ion. The flux surface average of the parallel ion heat flux is represented by the term $\left\langle u_{2\parallel i}\right\rangle$ (see Appendix A). We have used the notations of [12]:

$$b^2 = B^2/\left\langle B^2\right\rangle \tag{6}$$

$$n = n_a/\langle n_a\rangle \tag{7}$$

If the neoclassical friction is large, as is usually the case, we can approximate the flux function $u(\psi)$ (see Appendix A)

$$u(\psi) \approx -\left(C_0^a + k_i\right)\frac{F}{\langle B^2\rangle}\frac{T_i}{e_i}\left(\partial_\psi \ln T_i + \frac{e_i}{T_i}\frac{\left\langle u_{2\parallel i}\right\rangle}{F}\right) \tag{8}$$

with k_i the neoclassical ion coefficient that sets the poloidal ion flow, with an asymptotic value in the banana regime that is $k_i \approx -1.17$ (see [24]). In the case of a heavy impurity with the main ion in the banana regime, we have $C_0^a + k_i \approx 0.33$, but this value can be significantly different depending on the radial position and the plasma parameters that are considered (see section 3.2).

In the large aspect ratio approximation, we get

$$u(\psi) \approx \, -\frac{C_0^a + k_i}{\langle B^2 \rangle} \frac{T_i}{e_i} \frac{q^*}{\epsilon} \left(\partial_r \ln T_i + \frac{e_i}{T_i} \frac{\epsilon}{q^*} \left\langle u_{2\|i} \right\rangle \right) \tag{9}$$

with $\epsilon = r/R$ and $q^* = rB_0/\partial_r\psi$ with B_0 the magnetic field at the magnetic axis, and with the notations $\tilde{\mathcal{G}} = (rB_0/q^*)\,\mathcal{G}$ and $\tilde{\mathcal{U}} = (rB_0/q^*)\,\mathcal{U}$ we have

$$\tilde{\mathcal{G}} = \partial_r \ln p_a - \frac{e_a}{e_i} \frac{T_i}{T_a} \partial_r \ln p_i + C_0^a \frac{e_a}{e_i} \frac{T_i}{T_a} \partial_r \ln T_i \tag{10}$$

$$\tilde{\mathcal{U}} = \, - \left(C_0^a + k_i \right) \frac{e_a}{e_i} \frac{T_i}{T_a} \left(\partial_r \ln T_i + \frac{e_i}{T_i} \frac{\epsilon}{q^*} \left\langle u_{2\|i} \right\rangle \right) \tag{11}$$

The poloidal asymmetry is separated into horizontal (δ) and vertical (Δ) components (see [12]), so that we have:

$$b = 1 - \epsilon \cos\theta \tag{12}$$

$$n = 1 + \delta \cos\theta + \Delta \sin\theta \tag{13}$$

Assuming δ and Δ to be the same order as ϵ, the radial impurity flux writes at lowest order in ϵ [12]:

$$\langle \Gamma_a \cdot \nabla r \rangle \approx \, - \langle n_a \rangle \; D_{PS}^a \left[\left(1 + \frac{\delta}{\epsilon} + \frac{\delta^2 + \Delta^2}{4\epsilon^2} \right) \tilde{\mathcal{G}} + \frac{1}{2} \left(\frac{\delta}{\epsilon} + \frac{\delta^2 + \Delta^2}{2\epsilon^2} \right) \tilde{\mathcal{U}} \right] \tag{14}$$

with $D_{PS}^a \equiv 2q^{*2} m_a \nu_a T_a / (e_a^2 \langle B^2 \rangle)$. Note that due to the dependence $\nu_a \approx \nu_i (Z_a/Z_i)^2 m_i/m_a$ with ν_i the ion-ion collision frequency, the diffusion coefficient D_{PS}^a is comparable for all impurity species if we assume that they have the same temperature. For the comparison with numerical simulations, we will consider different approximations of the theoretical value of the radial impurity velocity $V_{a,r}^{th} = \langle \Gamma_a \cdot \nabla r \rangle / \langle n_a \rangle$:

$$V_{a,r}^{th\,(0)} = \, - D_{PS}\, \tilde{\mathcal{G}} \tag{15}$$

$$V_{a,r}^{th\,(1)} = \left(1 + \frac{\delta}{\epsilon} + \frac{\delta^2 + \Delta^2}{4\epsilon^2} \right) V_{a,r}^{th\,(0)} \tag{16}$$

$$V_{a,r}^{th\,(2)} = V_{a,r}^{th\,(1)} + D_{PS} \frac{C_0^a + k_i}{2} \frac{e_a}{e_i} \frac{T_i}{T_a} \left(\frac{\delta}{\epsilon} + \frac{\delta^2 + \Delta^2}{2\epsilon^2} \right) \partial_r \ln T_i \tag{17}$$

The first evaluation $V_{a,r}^{th\,(0)}$ ignores all poloidal asymmetries, the second one $V_{a,r}^{th\,(1)}$ takes them into account but assumes $u(\psi) = 0$, the third one takes into account asymmetries and $u(\psi)$, but assumes that $\left\langle u_{2\|i} \right\rangle = 0$.

2.1.2. Impurity flux for a poloidally asymmetric main ion density In the case where the ion density is not a flux function, the neoclassical impurity flux can be expressed as:

$$\langle \Gamma_a \cdot \nabla\psi \rangle = m_a \nu_a \frac{F^2 T_a \langle n_a \rangle}{e_a^2 \langle B^2 \rangle} \left[\left(\frac{1}{\left\langle \frac{b^2}{n} \right\rangle} - \left\langle \frac{n}{b^2} \right\rangle \right) \mathcal{G} + \left(\frac{\left\langle \frac{b^2}{N} \right\rangle}{\left\langle \frac{b^2}{n} \right\rangle} - \left\langle \frac{n}{N} \right\rangle \right) \mathcal{U} \right] \tag{18}$$

with $N = n_i/\langle n_i\rangle$ the asymmetry of the main ion density. Using the notation $N = 1+\delta_N\cos\theta+\Delta_N\sin\theta$, we arrive to

$$\begin{aligned}\langle\Gamma_a\cdot\nabla r\rangle \approx\ & -\langle n_a\rangle\ D^a_{PS}\left[\left(1+\frac{\delta}{\epsilon}+\frac{\delta^2+\Delta^2}{4\epsilon^2}\right)\tilde{\mathcal{G}}\right.\\ &\left.+\frac{1}{2}\left(\frac{\delta-\delta_N}{\epsilon}+\frac{\delta^2+\Delta^2-\delta\delta_N-\Delta\Delta_N}{2\epsilon^2}\right)\tilde{\mathcal{U}}\right]\end{aligned} \tag{19}$$

A simplified expression, to be compared with equation (17), can be derived with the assumption $\langle u_{2\|i}\rangle = 0$:

$$\begin{aligned}V^{th\,(2)}_{a,r}(N,\phi)\approx\ & -D^a_{PS}\left(1+\frac{\delta}{\epsilon}+\frac{\delta^2+\Delta^2}{4\epsilon^2}\right)\tilde{\mathcal{G}}\\ &+D^a_{PS}\frac{C^a_0+k_i}{2}\frac{e_a}{e_i}\frac{T_i}{T_a}\left(\frac{\delta-\delta_N}{\epsilon}+\frac{\delta^2+\Delta^2-\delta\delta_N-\Delta\Delta_N}{2\epsilon^2}\right)\partial_r\ln T_i\end{aligned} \tag{20}$$

where the asymmetry (δ,Δ) now depends not only on the asymmetry of the ion density but also on that of the electrostatic potential ϕ as will now be shown.

2.2. Poloidal distribution

In the general case, the poloidal variation of the impurity density (see Appendix A) is determined by :

$$\partial_\theta\ln n_a+\frac{e_a}{T_a}\partial_\theta\phi = JF\frac{m_a\nu_a}{e_a}\left[\left(1-\frac{b^2}{n\left\langle\frac{b^2}{n}\right\rangle}\right)\mathcal{G}+\left(\frac{b^2}{N}-\frac{b^2}{n}\frac{\langle b^2/N\rangle}{\langle b^2/n\rangle}\right)\mathcal{U}\right] \tag{21}$$

with J the Jacobian of the co-ordinate system (ψ,θ,φ) and ϕ the electrostatic potential.

2.2.1. Poloidally homogeneous ion density and electrostatic potential We can identify the terms in $\cos\theta$ and $\sin\theta$ of the poloidal distribution of the impurity (see equation 13) and we obtain from equation (21), where $N = 1$, $\partial_\theta\phi = 0$:

$$\Delta = \mathcal{A}\left[\mathcal{G}\left(2\epsilon+\delta\right)+\mathcal{U}\delta\right] \tag{22}$$

$$\delta\ =\ -\mathcal{A}\left(\mathcal{G}+\mathcal{U}\right)\Delta \tag{23}$$

with $\mathcal{A} = JF\,m_a\nu_a/e_a$. Note that we neglect higher order terms in δ^2, Δ^2 or $\epsilon\delta$ from the right hand side of equation (21). Due to the dependence $\nu_a \propto e_a^2/m_a$ (to leading order), the parameter $\mathcal{A}$ scales linearly with the impurity charge, and the impurity mass has a negligible influence. The above relations show that the horizontal (δ) and vertical (Δ) asymmetries are related through

$$\Delta^2+\left(\delta-C_\delta\right)^2 = R^2_\Delta \tag{24}$$

which describes a circle of center C_δ and radius R_Δ with

$$C_\delta\ =\ -\epsilon/\left(1+\mathcal{U}/\mathcal{G}\right) \tag{25}$$

$$R_\Delta = \left|\epsilon/\left(1+\mathcal{U}/\mathcal{G}\right)\right| \tag{26}$$

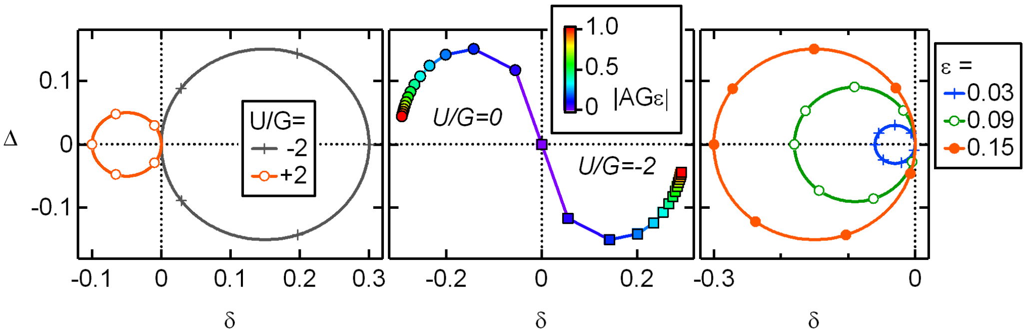

Figure 1. Poloidal asymmetry circle: influence of the equilibrium gradients where $\mathcal{U}/\mathcal{G} < 0$ is typical of a flat ion density profile and $\mathcal{U}/\mathcal{G} \geq 0$ of a peaked ion density profile ($\epsilon = 0.15$, left plot); influence of collisionality ($\epsilon = 0.15$, middle plot); influence of radial position ($\mathcal{U}/\mathcal{G} = 0$, right plot)

The position of the center C_δ depends on the sign of $1+\mathcal{U}/\mathcal{G}$. We have for $T_a = T_i$, $e_a \gg e_i$ and neglecting the flux-averaged parallel heat flux:

$$1+\mathcal{U}/\mathcal{G} \approx \frac{\partial_r \ln n_i + (1+k_i)\,\partial_r \ln T_i}{\partial_r \ln n_i + (1-C_0^a)\,\partial_r \ln T_i} \tag{27}$$

If the ion density profile is flat, then the position depends on the sign of $(1+k_i)\,/\,(1-C_0^a)$. This sign is negative in usual cases because ions are often not deeply in the banana regime and (k_i+1) is positive. In that case, the center C_δ is at $\delta > 0$. If on the contrary the density profile is peaked, then $1+\mathcal{U}/\mathcal{G} \approx 1$ and the center is at $\delta < 0$ (figure 1, left panel).

We can define the angular position α that results from the collisional drive

$$\delta\ = C_\delta + R_\Delta \cos\alpha \tag{28}$$

$$\Delta = R_\Delta \sin\alpha \tag{29}$$

and we have

$$\cos\alpha = \frac{R_\Delta}{C_\delta}\frac{(\mathcal{AG}\epsilon)^2 - R_\Delta^2}{(\mathcal{AG}\epsilon)^2 + R_\Delta^2} \tag{30}$$

$$\sin\alpha\ = 2R_\Delta \frac{\mathcal{AG}\epsilon}{(\mathcal{AG}\epsilon)^2 + R_\Delta^2} \tag{31}$$

If the equilibrium gradients are such that $\mathcal{G} > 0$, then $\sin\alpha > 0$ and the vertical asymmetry Δ is positive. This situation is typically encountered for a peaked ion density profile. For a flat density profile, we have $\mathcal{G} < 0$ and the vertical asymmetry Δ is negative. When the collisionality increases (figure 1, middle panel), the asymmetry moves away from 0 following the circle defined by (C_δ, R_Δ, α), but the sign of the vertical asymmetry does not change. Due to the dependence on ϵ of the circle radius, the amplitude of the asymmetry increases with the minor radius (figure 1, right panel).

With this model for impurity flux and asymmetry, one can estimate the impurity that will be transported the fastest for a given equilibrium. For example, using an

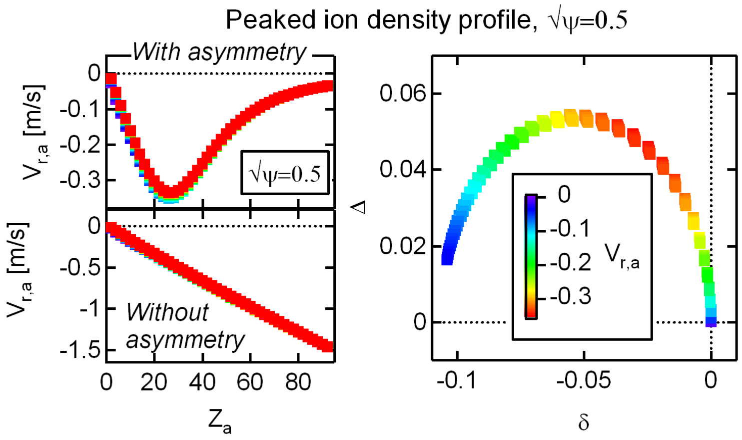

Figure 2. Role of the impurity charge and mass : radial velocity as a function of the ion charge (left plot), with poloidal asymmetry (top) and without (bottom), and vertical asymmetry as a function of horizontal asymmetry (right plot), for the peaked ion density profile decribed in section 3.2, and for a flat impurity profile. The different points for each impurity charge correspond to different masses.

equilibrium with a peaked ion density profile and a flat impurity profile that will be described in section 3.2, we can compute the radial flux for a large set of impurity mass and charge, taking into account the poloidal asymmetry. This is shown in figure 2, where we cover the range $Z_a \in [2,\ 92]$ and $m_a/m_p \in [10,\ 186]$ with m_p the proton mass. The impurity that is transported inwards with the fastest velocity has a charge in the range 20 to 30. This corresponds to a maximum of the vertical asymmetry, and this can be understood when the impurity flux is expressed as a function of $(C_\delta,\ R_\Delta,\ \alpha)$:

$$\frac{2R_\Delta \tilde{\mathcal{A}} \epsilon}{\left(\tilde{\mathcal{A}}\tilde{\mathcal{G}}\epsilon\right)^2 + R_\Delta^2} \left\langle \Gamma_a \cdot \nabla r \right\rangle = -\left\langle n_a \right\rangle D_{PS} \sin\alpha \left[1 + \frac{\delta}{2\epsilon} - \frac{\delta}{2C_\delta} - \frac{\delta^2 + \Delta^2}{4\epsilon C_\delta}\right] \tag{32}$$

where the poloidal asymmetry parameters $(\delta,\ \Delta)$ are functions of $(C_\delta,\ R_\Delta,\ \alpha)$ and $\tilde{\mathcal{A}} = q^*/(rB_0)\mathcal{A}$. To leading order, the amplitude of the flux is maximized when $\alpha \approx \pm\pi/2$ and then the vertical asymmetry is also an extremum. Note that the mass of the impurity plays a minor role in its radial neoclassical transport when rotation can be neglected.

2.2.2. Poloidally inhomogeneous ion density and electrostatic potential We now assume some poloidal asymmetry of the ion density and of the electrostatic potential. We note:

$$\frac{e\phi}{T_e} = \frac{e\left\langle \phi \right\rangle}{T_e} + \delta_\phi \cos\theta + \Delta_\phi \sin\theta \tag{33}$$

and for each impurity we note $\left(\delta_\phi^a,\ \Delta_\phi^a\right) = Z_a(T_e/T_a)\left(\delta_\phi,\ \Delta_\phi\right)$.

The identification of cosine and sine terms of the impurity asymmetry in equation

(21) leads to (see Appendix A):

$$\Delta + \Delta_\phi^a = \mathcal{A}\left[(2\epsilon + \delta)\,\mathcal{G} + (\delta - \delta_N)\,\mathcal{U}\right] \tag{34}$$

$$\delta + \delta_\phi^a \;=\; -\,\mathcal{A}\left[\Delta\mathcal{G} + (\Delta - \Delta_N)\,\mathcal{U}\right] \tag{35}$$

The circle has now a shifted center and does not intersect the origin in general:

$$(\delta - C_\delta)^2 + (\Delta - C_\Delta)^2 \;=\; R_\Delta^2 \tag{36}$$

Its characteristics are changed into:

$$C_\delta \;= C_\delta^0\left(1 - \frac{\delta_N}{2\epsilon}\frac{\mathcal{U}}{\mathcal{G}}\right) - \frac{\delta_\phi^a}{2} \tag{37}$$

$$C_\Delta = -\,\frac{\Delta_\phi^a}{2} - C_\delta^0\frac{\Delta_N}{2\epsilon}\frac{\mathcal{U}}{\mathcal{G}} \tag{38}$$

$$R_\Delta^2 = \left|C_\delta^0\right|^2\left[1 + \frac{\delta_\phi^a}{C_\delta^0} - \frac{\delta_N}{\epsilon}\frac{\mathcal{U}}{\mathcal{G}} + \left(\frac{\delta_\phi^a}{2C_\delta^0} - \frac{\delta_N}{2\epsilon}\frac{\mathcal{U}}{\mathcal{G}}\right)^2 + \left(\frac{\Delta_\phi^a}{2C_\delta^0} - \frac{\Delta_N}{2\epsilon}\frac{\mathcal{U}}{\mathcal{G}}\right)^2\right] \tag{39}$$

with $C_\delta^0 = -\epsilon/(1+\mathcal{U}/\mathcal{G})$ the center of the circle when only the asymmetry of the impurity is considered. The collisional angle α can then be determined in the general case :

$$\delta \;= C_\delta + R_\Delta\cos\alpha \tag{40}$$

$$\Delta = C_\Delta + R_\Delta\sin\alpha \tag{41}$$

with

$$\cos\alpha = \frac{R_\Delta C_\delta^0}{\mathcal{D}}\left\{\left[\left(\frac{\mathcal{AG}\epsilon}{C_\delta^0}\right)^2 - 1\right]\left(1 + \frac{\delta_\phi^a}{2C_\delta^0} - \frac{\delta_N}{2\epsilon}\frac{\mathcal{U}}{\mathcal{G}}\right) + \frac{\mathcal{AG}\epsilon}{C_\delta^0}\left[\frac{\Delta_N}{\epsilon}\frac{\mathcal{U}}{\mathcal{G}} - \frac{\Delta_\phi^a}{C_\delta^0}\right]\right\} \tag{42}$$

$$\sin\alpha \;= \frac{R_\Delta C_\delta^0}{\mathcal{D}}\left\{\left[\left(\frac{\mathcal{AG}\epsilon}{C_\delta^0}\right)^2 - 1\right]\left(\frac{\Delta_\phi^a}{2C_\delta^0} - \frac{\Delta_N}{2\epsilon}\frac{\mathcal{U}}{\mathcal{G}}\right) + \frac{\mathcal{AG}\epsilon}{C_\delta^0}\left(2 + \frac{\delta_\phi^a}{C_\delta^0} - \frac{\delta_N}{\epsilon}\frac{\mathcal{U}}{\mathcal{G}}\right)\right\} \tag{43}$$

and $\mathcal{D} = (\mathcal{AG}\epsilon)^2\,(R_\Delta/C_\delta^0)^2 + R_\Delta^2$.

As an illustration, we show in figure 3 the variation of the radial velocity and poloidal asymmetry of Tungsten W^{44+} and Carbon C^{6+} for the peaked ion density case at $\sqrt{\psi} = 0.5$, as a function of δ_ϕ and Δ_ϕ. Here we assume that the ion density and electrostatic potential asymmetries are related by $(\delta_N, \Delta_N) = -(\delta_\phi^i, \Delta_\phi^i)$ [18]. The radial velocity varies with a parabolic shape as a function of δ_ϕ, as evidenced in the case of Tungsten. The horizontal asymmetry of the impurity varies in the direction opposite to that of the electrostatic potential, due to the displacement of the center C_δ, and can change sign.

In the situations that we consider in the numerical simulations, the poloidal asymmetry of the electrostatic potential is much smaller than the range of values covered in figure 3, with $|\delta_\phi|$ below 0.1% and $|\Delta_\phi|$ below 0.02% inside $\sqrt{\psi} = 0.8$. However, we will see that the contribution of the electrostatic potential is measurable, in particular regarding the modification of the poloidal asymmetry of light impurities.

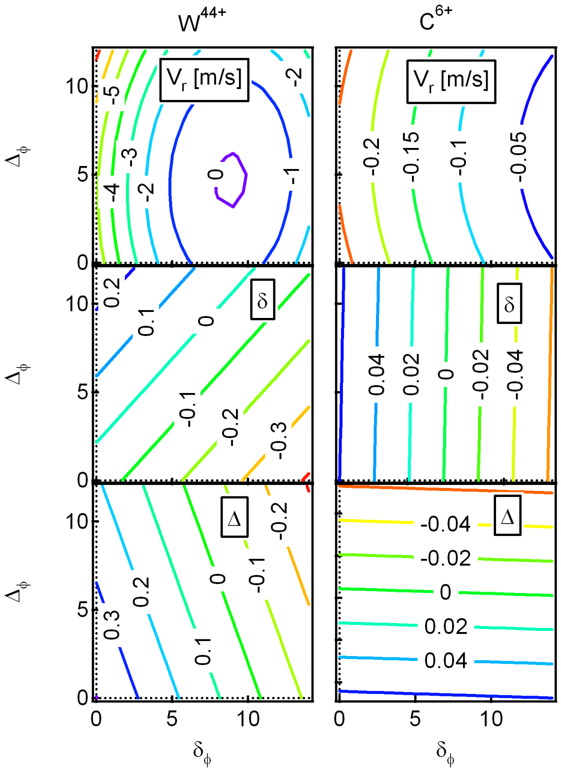

Figure 3. Influence of the asymmetry of the electrostatic potential on W^{44+} (left column) and C^{6+} (right column). From top to bottom: radial velocity, horizontal symmetry, and vertical asymmetry, for the peaked ion density profile case at $\sqrt{\psi} = 0.5$.

2.3. Equilibrium impurity profile

The impurity flux (eq. 14) can be expressed as a function of $(C_\delta,\ R_\Delta,\ \alpha)$, where the parameters can be computed from the impurity and ion gradients contained in $\mathcal{G}$ and $\mathcal{U}$. This allows deriving the equilibrium (in the sense of stationnary) impurity profile in an iterative process:

(i) The gradients $\mathcal{G}$ and $\mathcal{U}$ are computed from an initial impurity profile

(ii) The circle center and radius are deduced from equations (25) and (26)

(iii) The angle on the circle is determined using the relations (30) and (31), and the asymmetries using equations (28) and (29)

(iv) The impurity flux can then be computed using equation (14) and the equilibrium conditions ($\langle \Gamma_a \cdot \nabla r \rangle = 0$) provides a new value for $\mathcal{G}$ and therefore for the impurity gradient (we recall that the impurity is assumed to be a trace and therefore it does not interfere with the ambipolarity condition).

(v) By allowing only a fraction of the variation of impurity gradient to be effective at each step, we obtain a progressive evolution of the impurity distribution, until the flux cancels.

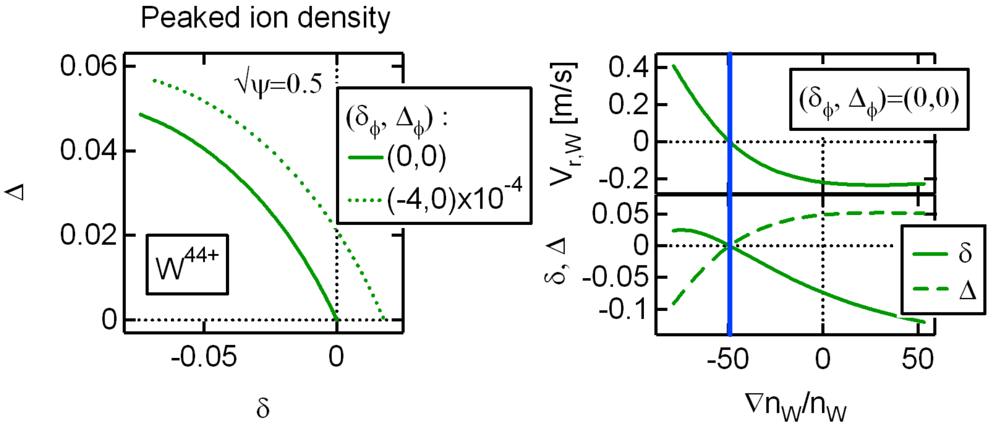

Figure 4. Left : Influence of the asymmetry of the electrostatic potential on the trajectory of the poloidal asymmetry towards steady state, for W^{44+} in the peaked ion density profile case at $\sqrt{\psi} = 0.5$. Right: Radial Tungsten velocity (top) and asymmetry (δ, Δ) as a function of the normalized Tungsten density gradient for $(\delta_\phi, \Delta_\phi) = (0, 0)$. At the equilibrium point ($V_{r,W} = 0$, indicated by a blue vertical line), the asymmetry also cancels.

This procedure will be used in section 4.4 for establishing the expected trajectory of the poloidal asymmetry in the $(\delta,\ \Delta)$ plane, and compare it with the simulations.

From the circle equation (24) and the condition that the flux vanishes (equation 14) we obtain that $\Delta = 0$ at equilibrium, i.e. the equilibrium poloidal distribution has no vertical asymmetry. This leads also, using equations (22) (23) and (31), to $\delta = 0$, and $\mathcal{G} = 0$, i.e. the impurity poloidal distribution at equilibrium has no asymmetries and the impurity profile converges to its neoclassical value without asymmetries. This can be verified by applying the above procedure, as shown in the left plot of figure 4, or by performing a scan in the impurity gradient length, as shown in the right plot of the same figure (the equilibrium profiles are taken here from the peaked ion density profile that will be described later).

In the presence of a poloidal asymmetry of the electrostatic potential, the steady state impurity concentration has a remaining poloidal asymmetry itself. To illustrate this, we show in figure 4 the trajectory of the poloidal asymmetry of Tungsten W^{44+} for a poloidally symmetric electrostatic potential and for $(\delta_\phi,\ \Delta_\phi) = (-4 \times 10^{-4},\ 0)$. We assume again that $(\delta_N, \Delta_N) = -(\delta^i_\phi, \Delta^i_\phi)$. This example shows that even a small asymmetry of the electrostatic potential has a considerable effect on the steady state asymmetry of highly charged impurities.

3. Model and settings

3.1. MHD model

The numerical tool that we use is the XTOR code [20] with the drift-neoclassical model described in [21] where we have made corrections detailed in [25]. The model is completed with two additional equations per impurity, describing particle conservation and parallel momentum:

$$\partial_t n_a + \nabla \cdot (n_a \mathbf{V_a}) = \nabla \cdot D_a \nabla n_a + \Sigma_a \tag{44}$$

$$m_a n_a D_t V_{a\|} = -\nabla_\| p_a + n_a e_a E_\| + R_{a\|} - \left(\nabla \cdot \Pi_a\right)_\| \tag{45}$$

with $D_t \equiv \partial_t + \left[\left(V_{\|a}\mathbf{b} + \mathbf{V_E}\right) \cdot \nabla V_{\|a}\mathbf{b}\right] \cdot \mathbf{b}$ and where we assume $E_\| \approx -\nabla_\| p_e/(en_e)$, $R_{a\|}$ is the parallel component of the collisional friction force and $\left(\nabla \cdot \Pi_a\right)_\|$ is the parallel component to the anisotropic pressure tensor (see Appendix B). This implementation is similar to that used in [23], except for the parallel ion heat flux that is connected here with the neoclassical closure. All components of the radial impurity flux (classical, banana-plateau and Pfirsch-Schlüter) are included in this model, although the Pfirsch-Schlüter one remains dominant in the simulations, as can be verified by artificially removing the anisotropic pressure tensor.

The collision frequency between the impurity and the main ion (the coefficient ν_a in equation 1) is normalized to the Alfvén time, and it can be multiplied by a free factor α_ν. This free factor is used in the present study for investigating the collisionality dependence of the impurity flux. The impurity species are considered as traces and do not interact with the main plasma evolution.

3.2. Equilibrium and other settings

The equilibrium that is considered is a low pressure, circular cross-section tokamak equilibrium, with a monotonic safety factor profile, computed with the equilibrium code CHEASE [26]. It has an inverse aspect ratio $\epsilon = 0.3$, the pressure profile is given by $\partial_\psi p \propto (1-\psi)$ and the current density profile by $I^* \propto (1-\psi)^2$ (see [26] for the definition of I^*). At magnetic axis ($R_0 = 2.4m$), the magnetic field is $B_0 = 3T$, the ion density $n_i(0) = 4 \times 10^{19} m^{-3}$, electron temperature $T_e(0) = 1954eV$, and $\tau \equiv T_i/T_e = 1$, these quantities being chosen so that they are consistent with the CHEASE equilibrium : $p(0) = en_i(0)T_e(0)\ [1+\tau]$. The ion density profile is parametrized with

$$n_i(\psi)/n_i(0) = \frac{1 - d_1\psi^{d_2}}{1 + d_3\psi^{d_4}} \tag{46}$$

Two different ion density profiles are considered:

- Nearly flat density profile : $(d_1, d_2, d_3, d_4) = (0.1, 1, 0.1, 1)$
- Peaked density profile : $(d_1, d_2, d_3, d_4) = (0.5, 2, 2, 1.5)$

the first one leading to an outward impurity flux, and the second one to an inward impurity flux. The magnetic equilibrium being fixed, this leads to slightly different

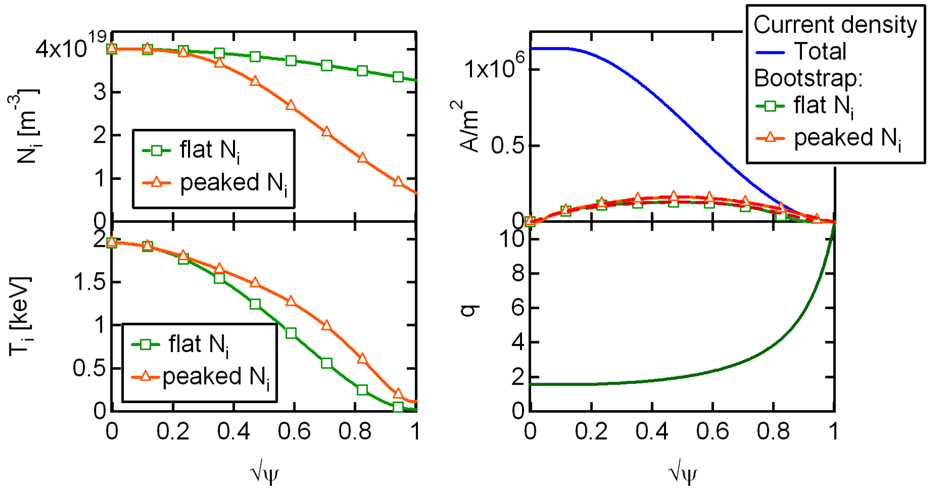

Figure 5. Left : ion density (top) and temperature (bottom) profiles for the two reference cases. Right: total and bootstrap current densities (top) and safety factor profile (bottom).

temperature profiles (see figure 5). Note that the code computes the bootstrap current as part of its neoclassical outputs, as shown in figure 5.

In the study we investigate the dynamics of two different trace species. One is a light impurity, the Carbon ${}^{12}_{6}\mathrm{C}^{6+}$, and the other is Tungsten ${}^{184}_{74}\mathrm{W}^{44+}$, a heavy one that is of particular concern for fusion research since plasma facing components made with this material receive the peak heat flux in the divertors of JET [27], ASDEX-Upgrade [28], EAST [29] and WEST [30], anticipating the situation of ITER [31]. The profile of the coefficient k_i , computed in XTOR (as all other neoclassical coefficients) from the model described in [32], is shown in figure 6. We have $C_0^W \approx 1.48$ and $C_0^C \approx 1.29$, so that in the outer part of the plasma, where $k_i > 0$, the weight of the ion temperature gradient in the determination of the impurity flux is much larger than could be anticipated in the banana regime approximation $C_0^a + k_i = 0.33$. Note finally that the initial profile of these impurities is flat, with a central value that represents a fraction 10^{-6} of the central ion density.

Since we want to study the neoclassical part of impurity transport, we set a very low value for the anomalous diffusion coefficient $D_{\perp,a}$, much lower than $D_{PS,a}$. We take a constant value $D_{\perp,a} = 0.0016\, m^2/s$ in all the simulations (except during a short phase in the long term evolution presented in section 4.4). The profiles of both quantities are shown in figure 6. The central Lundquist number used in the simulations is $S_0 = 10^8$ (about half the value consistent with plasma parameters), and we take $S\chi_\perp = 10^3$, $\chi_\parallel/\chi_\perp = 10^8$ and $D_\perp = 2/3\, \chi_\perp$.

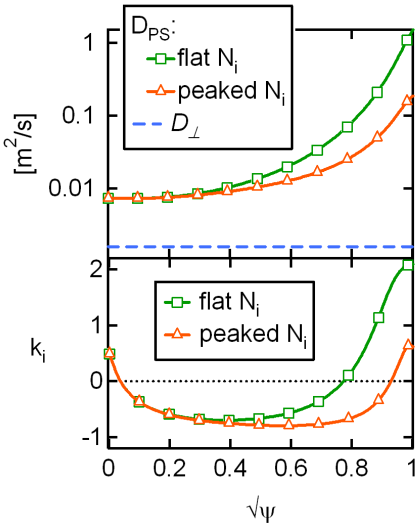

Figure 6. Diffusion coefficients D_{PS} and $D_\perp$ (top), and neoclassical parameter k_i (bottom) for the peaked and nearly flat ion density cases.

4. Impurity flux of trace impurities and comparison with analytical estimates

4.1. Determination of particle fluxes and other diagnostics

The impurity particle flux is determined from the dynamics of the axisymmetric component of the impurity density n_a. From

$$\partial_t n_a + \nabla \cdot \Gamma_a = 0 \tag{47}$$

we get

$$\partial_t N_a + \langle \Gamma_a \rangle S_\psi = 0 \tag{48}$$

with S_ψ the area of the flux surface considered and

$$N_a \equiv \int dV n_a \tag{49}$$

$$\langle \Gamma_a \rangle \equiv S_\psi^{-1} \int \mathbf{\Gamma_a} \cdot \mathbf{dS}_\psi \tag{50}$$

From this we compute the radial velocity $V_{r,a} = \langle \Gamma_a \rangle / \langle n_a \rangle$.

We will use a criterion to evaluate the conditions where the poloidal asymmetry will be large, by computing a simplified form of the vertical asymmetry Δ [23]:

$$C = 2Rq^2 \frac{m_a}{m_i} \frac{\nu_a}{\Omega_i} \left| \partial_r \ln n_i - (C_0^a - 1) \partial_r \ln T_i \right| \tag{51}$$

with $\Omega_i = e_i B_0 / m_i$ the ion cyclotron frequency. The poloidal asymmetry is expected to be unimportant whenever $C \ll 1$. This criterion is useful for estimating the range over which α_ν can be varied without loosing the linear dependence of the particle flux with respect to the collisionality. For example, in a simulation with a low Lundquist number, the current diffusion is accelerated compared to reality, and one would like to accelerate in a consistent way the particle fluxes. This will be possible only if the criterion in equation (51) remains small compared to unity.

The poloidal asymmetry of the electrostatic potential can be evaluated in the simulation by computing

$$\partial_\theta \phi = -\frac{JB^2}{F}\mathbf{v_E}\cdot\nabla\psi \tag{52}$$

$$\delta_\phi = -\frac{e}{2T_e}\left[\partial_\theta\phi(\theta=\pi/2) - \partial_\theta\phi(\theta=-\pi/2)\right] \tag{53}$$

$$\Delta_\phi = \frac{e}{2T_e}\left[\partial_\theta\phi(\theta=0) - \partial_\theta\phi(\theta=\pi)\right] \tag{54}$$

This asymmetry can be related through the parallel Ohm's law to the electron density, in the limit where plasma resistivity can be neglected:

$$E_\parallel \approx -\frac{\nabla_\parallel p_e}{en_e} \tag{55}$$

$$\frac{e}{T_e}\partial_\theta\phi \approx \partial_\theta \ln n_e \tag{56}$$

In principle, the asymmetry of the main ion density should be opposite to that of the electrostatic potential [18], but we evolve only the ion density in the code, assuming quasineutrality with a trace impurity: $n_e = Z_i n_i$. We have therefore $(\delta_N,\, \Delta_N) \approx (\delta_\phi,\, \Delta_\phi)$, as can be verified in the simulations.

4.2. Impurity flux as a function of collisionality

We perform simulations where the impurity collision frequency is amplified by the arbitrary factor α_ν (see section 3.1), from $\alpha_\nu = 8$ down to $\alpha_\nu = 0.25$ (for the peaked density case) or $\alpha_\nu = 0.1$ (for the flat density case). The initial impurity profile is flat. Each value of the scan in α_ν is kept between 5 to 10 ms, which is generally long enough to stabilize the particles fluxes. We then compute the averaged quantities and the standard deviations over a period of 3 to 5 ms.

The evolution of the radial particle flux and of the asymmetry at $\sqrt{\psi} = 0.4$ are shown in figures 7 and 8 for the peaked and flat ion density cases respectively. The analytic evaluations of the flux ($V_{a,r}^{th\,(0)}$, $V_{a,r}^{th\,(1)}$ and $V_{a,r}^{th\,(2)}$) are computed from the theoretical density asymmetry without the contribution of the electrostatic potential, i.e. from equations (14), (28) and (29). For Carbon 6+, the different analytical evaluations are all similar and close to the numerical result because the level of asymmetry is always small. For Tungsten 44+, the situation is extremely different. At high collisionality, the radial flux is always very low, it passes through a maximum amplitude at lower collisionality and then converges towards the analytical estimate $V_{a,r}^{th\,(0)}$ at vanishing collisionality. The damping of the flux at large collisionality is inconsistent with the neoclassical evaluation without poloidal asymmetries, which are quite large in that regime with $\delta \sim 8\%$. When their role is considered without the $u(\psi)$ term ($V_{a,r}^{th\,(1)}$),

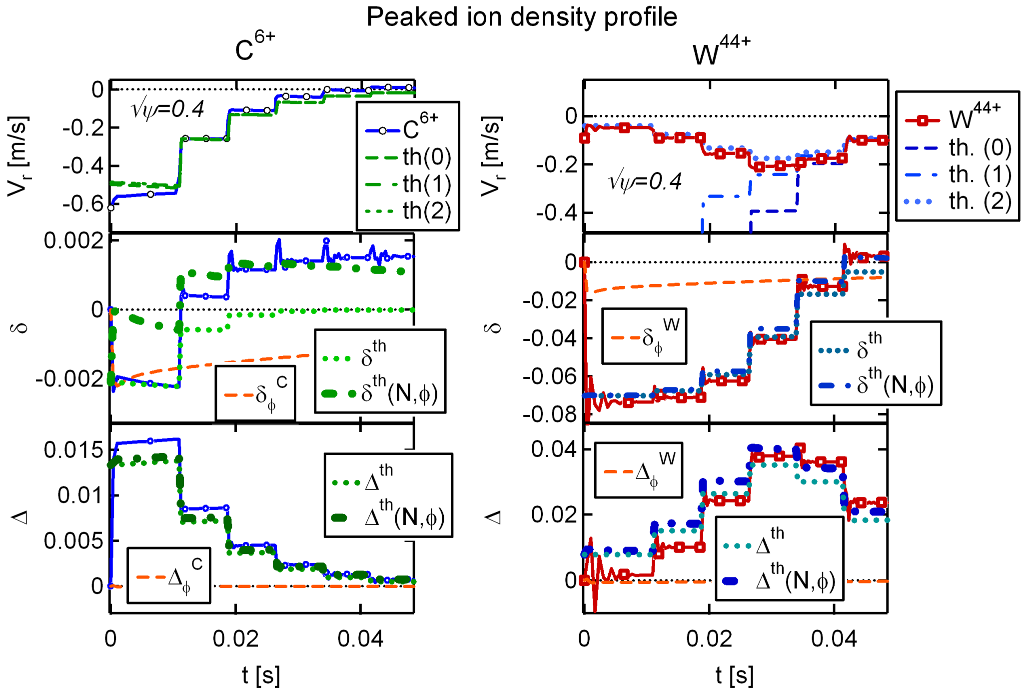

Figure 7. Peaked ion density profile : evolution of the radial particle flux (top), horizontal asymmetry δ (middle) and vertical asymmetry Δ (bottom) for C^{6+} (left) and W^{44+} (right) at $\sqrt{\psi} = 0.4$, during the collisionality scan (α_ν decreasing from 8 to 0.25 with the following steps : 8, 4, 2, 1, 0.5, 0.25). The asymmetry of the electrostatic potential (δ^a_ϕ, Δ^a_ϕ) is shown with dashed lines for the two impurities, as well as the predicted horizontal asymmetry without (δ^{th}) and with ($\delta^{th}(N,\phi)$) the contribution of poloidal asymmetries of the main ion density and of the electrostatic potential.

the agreement is improved only for the peak ion density profile, but for the flat ion density profile, where the ion temperature gradient contribution contained in the $u(\psi)$ term is dominant, the prediction is worse. Taking into account the $u(\psi)$ term, i.e. with $V^{th\,(2)}_{a,r}$, a good agreement is found either for the peaked or flat ion density cases, with a non monotonic variation of the Tungsten flux.

The evolution of the poloidal asymmetry is shown on the second and third plots of the two figures 7 and 8, together with the predicted asymmetry (δ^{th}, Δ^{th}). The prediction for Tungsten is satisfactory, with a non monotonic variation of the vertical asymmetry that follows that of the radial flux. For Carbon, we observe a change of sign for the horizontal asymmetry that cannot be explained without taking into account the contribution of the main ion and electrostatic potential asymmetries ($\delta^{th}(N,\phi), \Delta^{th}(N,\phi)$). We see indeed that the horizontal asymmetry of the electrostatic potential seen by Carbon, δ^C_ϕ, is comparable in amplitude to the measured asymmetry δ of the Carbon density. For Tungsten, we have δ^W_ϕ generally below the measured horizontal asymmetry of the density, except when the collisionality amplification is below unity ($\alpha_\nu < 1$) where it is comparable. We also measure in this case a change of sign of the horizontal asymmetry due to the contribution of the electrostatic potential,

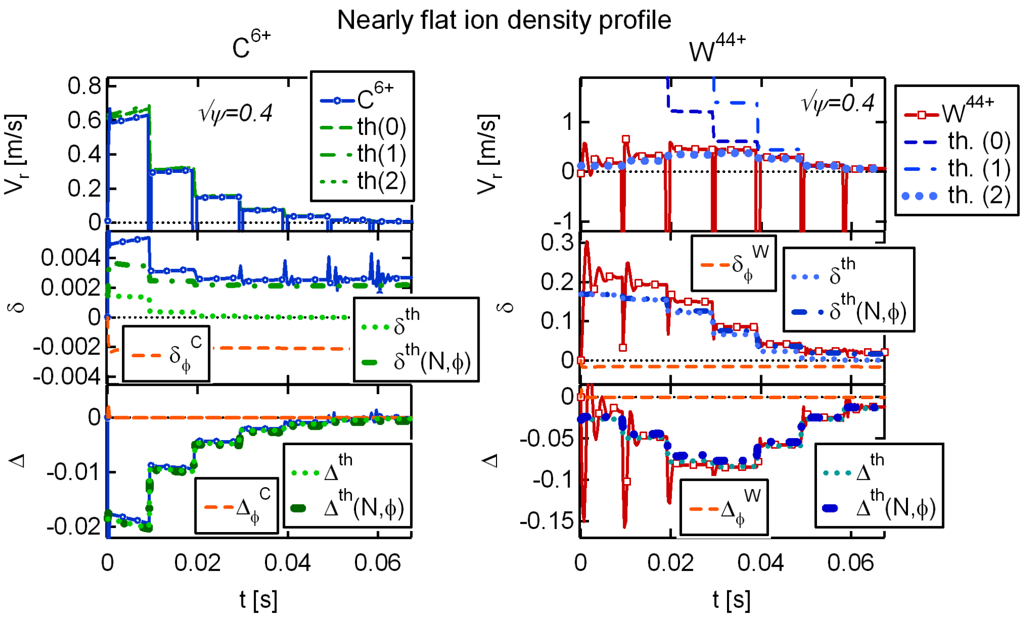

Figure 8. Flat ion density profile : evolution of the radial particle flux (top), horizontal asymmetry δ (middle) and vertical asymmetry Δ (bottom) for C^{6+} (left) and W^{44+} (right) at $\sqrt{\psi} = 0.4$, during the collisionality scan (α_ν decreasing from 8 to 0.1 with the following steps : 8, 4, 2, 1, 0.5, 0.25, 0.1). The asymmetry of the electrostatic potential (δ_ϕ^a, Δ_ϕ^a) is shown with dashed lines for the two impurities, as well as the predicted horizontal asymmetry without (δ^{th}) and with ($\delta^{th}(N,\phi)$) the contribution of poloidal asymmetries of the main ion density and of the electrostatic potential.

consistent with the prediction of the analytical model. However, it should be noted that in both cases the poloidal asymmetry is very low when the contribution of the electrostatic potential become of comparable amplitude, so that it has no significant impact on the flux. Note also that the dynamics of the electrostatic potential (which is decoupled from the impurity equations in our model), is relatively slow compared to the time scale of the scan that is performed, as can be seen in figure 7 in the plot relative to the horizontal asymmetry of Carbon. This could partly explain why the prediction that uses the information from the poloidal asymmetry of the main ion density and electrostatic potential, $\delta(N, \phi)$, is initially relatively far from the measured asymmetry. The agreement becomes satisfactory after 20 ms, but it also corresponds to a regime where the collisionality is lower.

The profiles of the radial particle velocity, asymmetry criterion (eq. 51), horizontal (δ) and vertical (Δ) asymmetries are shown in figures 9 and 10 for $\alpha_\nu = 1$. The impurity flux is directed outward when the ion density is flat and inward when it is peaked, in qualitative agreement with analytical estimates, except close to the edge where in all cases the poloidal asymmetry can be very large, and the analytical formula is no longer valid. The importance of poloidal asymmetries, as evaluated by the asymmetry criterion, is small for C^{6+}, except at the very edge. For W^{44+}, the criterion reaches unity around $\sqrt{\psi} = 0.6$ but the deviation of the radial velocity from $V_{a,r}^{th\,(0)}$ is visible already from

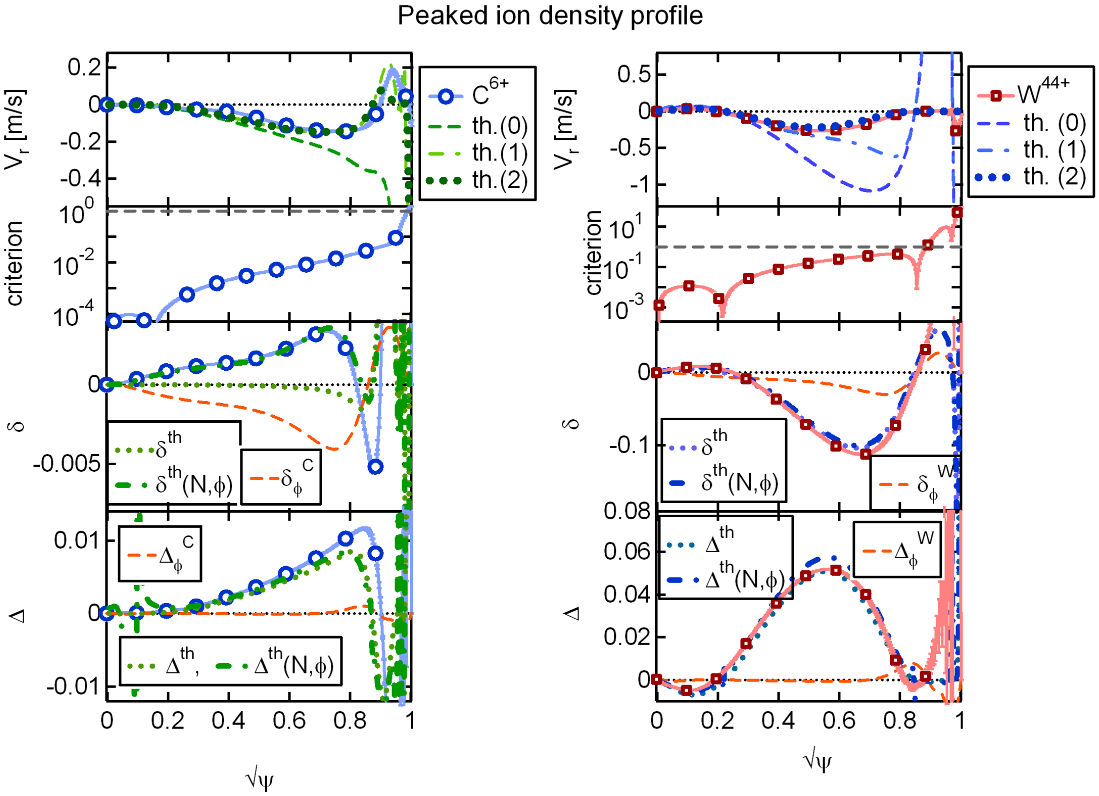

Figure 9. Peaked ion density profile, from top to bottom : profile of the radial particle velocity from the simulation and from analytical estimates, asymmetry criterion from equation (51), horizontal asymmetry and vertical asymmetry from the simulation and from analytical model with and without the contribution of the poloidal asymmetries of the main ion density and of the electrostatic potential, for C^{6+} (left) and W^{44+} (right), with $\alpha_\nu = 1$. Error bars on the measured quantities appears as a blue band for Carbon (left) and a red band for Tungsten (right).

$\sqrt{\psi} = 0.4$. This is clearly reflected in the different predictions of the impurity flux. In all cases, the analytical prediction $V_{a,r}^{th\,(2)}$ that takes into account the asymmetry and the $u(\psi)$ term is in good agreement with the simulations. It is interesting to detail how the horizontal asymmetry of Carbon depends on the electrostatic contribution. The theoretical prediction without the electrostatic potential is a nearly pure vertical asymmetry, but since δ_ϕ is negative, the Carbon density adopts a positive horizontal asymmetry, in agreement with the picture given in figure 3.

A closer look to the impurity flux behavior with respect to theory prediction is shown in figures 11 and 12 by plotting the ratio of the radial velocity to its analytical prediction $V_{a,r}^{th\,(0)}$ as a function of the collisional amplification factor α_ν (left plot), of the measured horizontal asymmetry (middle plot) and with respect to the asymmetry criterion (right plot). In the middle plot we also show the ratios $V_{a,r}^{th\,(1,2)}(N,\phi)/V_{a,r}^{th\,(0)}$ as a function of the measured horizontal asymmetry, and the contribution of the electrostatic potential is taken into account for evaluating the theoretical asymmetry (we use therefore formulas 37, 39, 42 and 43 for computing the theoretical radial velocity

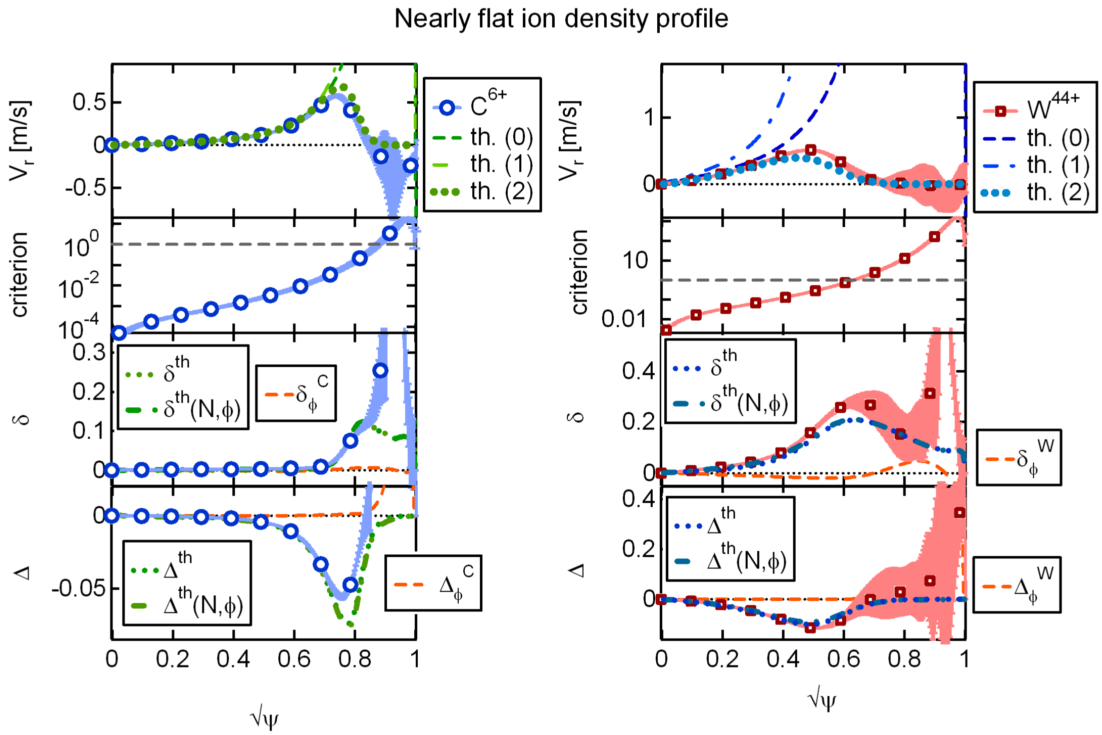

Figure 10. Flat ion density profile, from top to bottom : profile of the radial particle velocity from the simulation and from analytical estimates, asymmetry criterion from equation (51), horizontal asymmetry and vertical asymmetry from the simulation and from analytical model with and without the contribution of the poloidal asymmetries of the main ion density and of the electrostatic potential, for C^{6+} (left) and W^{44+} (right), with $\alpha_\nu = 1$. Error bars on the measured quantities appears as a blue band for Carbon (left) and a red band for Tungsten (right).

of equation 14). The contribution of the asymmetries of the main ion density and of the electrostatic potential is particularly important when the collisionality is reduced and δ becomes comparable to δ_ϕ^W. The colored area covers the domain bounded by $V_{a,r}^{th\,(1)}(N,\phi)/V_{a,r}^{th\,(0)}$ (upper bound) and $V_{a,r}^{th\,(2)}(N,\phi)/V_{a,r}^{th\,(0)}$(lower bound). It illustrates therefore the contribution of $u(\psi)$. The error bars that correspond to the standard deviation of the simulation results during the selected time window are greatly amplified in figure 12 because the theoretical value $V_{a,r}^{th\,(0)}$ that is at the denominator is getting close to zero at low collisionality.

For the peaked ion density profile, the reduction of the Tungsten flux by the poloidal asymmetry is well captured by $V_{a,r}^{th\,(1)}$, and the contribution of $u(\psi)$ is moderate. In contrast, when the ion density profile is nearly flat, the contribution of $u(\psi)$ reverses the dependence of the flux on the horizontal asymmetry.

The numerical simulation shows therefore that in the two cases that are considered, a peak or a flat ion density profile, the Tungsten flux is damped by the self consistent poloidal asymmetries that are generated by the friction with the main ions.

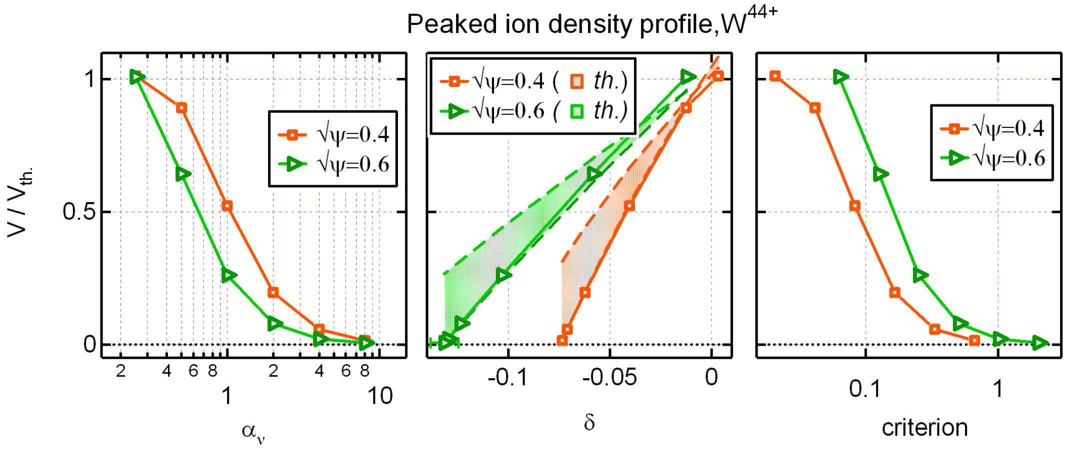

Figure 11. Peaked ion density profile : ratio of the radial velocity of Tungsten W^{44+} to its simplest theoretical estimate $V_{a,r}^{th\,(0)}$ as a function of the collisionality amplification factor α_ν (left), measured horizontal asymmetry δ (middle) and asymmetry criterion (right), at $\sqrt{\psi} = 0.4$ and 0.6 (at $\sqrt{\psi} = 0.2$, the theoretical value $V_{a,r}^{th\,(0)}$ is close to zero). In the middle plot, the green area is bounded by $V_{a,r}^{th\,(1)}(N,\phi)/V_{a,r}^{th\,(0)}$ (upper boundary) and $V_{a,r}^{th\,(2)}(N,\phi)/V_{a,r}^{th\,(0)}$ (lower boundary).

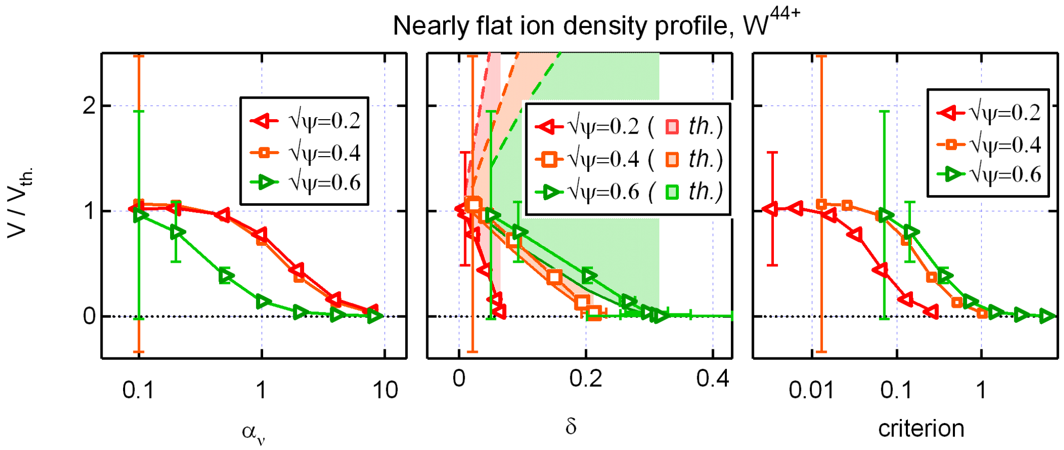

Figure 12. Nearly flat ion density profile : ratio of the radial velocity of Tungsten W^{44+} to its simplest theoretical estimate $V_{a,r}^{th\,(0)}$ as a function of the collisionality amplification factor α_ν (left), measured horizontal asymmetry δ (middle) and asymmetry criterion (right), at $\sqrt{\psi} = 0.2$, 0.4 and 0.6. In the middle plot, the green area is bounded by $V_{a,r}^{th\,(1)}(N,\phi)/V_{a,r}^{th\,(0)}$ (upper boundary) and $V_{a,r}^{th\,(2)}(N,\phi)/V_{a,r}^{th\,(0)}$ (lower boundary).

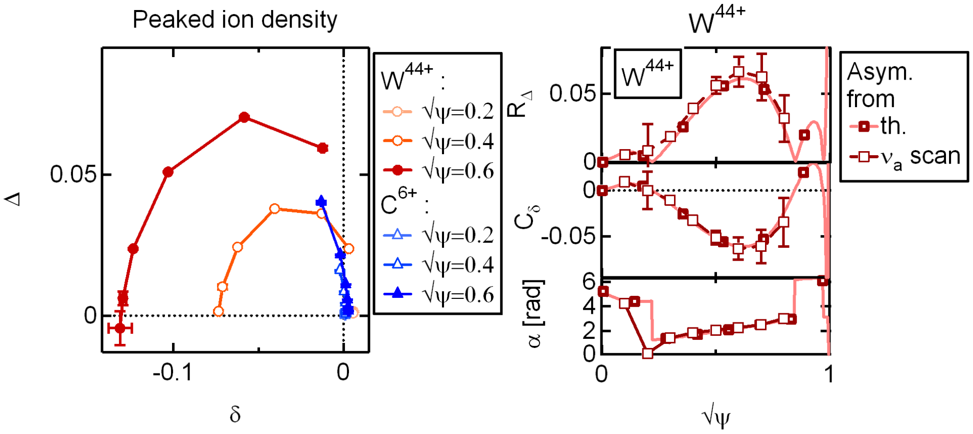

Figure 13. Trajectories of the W^{44+} and C^{6+} poloidal asymmetries at $\sqrt{\psi} = 0.2$, 0.4 and 0.6 (left), and comparison of the theoretical radius, center and collisional angle for W^{44+} at $\alpha_\nu = 1$ with its geometric determination during the collisionality scan (right), for the peaked ion density profile. The error bars correspond to the standard deviation of the evaluations made using equations (57) and (58).

4.3. Poloidal asymmetry and geometrical approach

The relation between horizontal and vertical asymmetries can be verified through the collisionality scan, since it is equivalent to a variation of the asymmetry angle α, on a circle with a fixed center and radius. On figures 13 and 14 we display for example the trajectory of the asymmetry at different radial positions for the two impurities, evidencing the geometrical dependencies illustrated in figure 1.

The analytical predictions for the position of the center of the circle, its radius and the angle α can also be compared with the numerical simulations. The center and radius of the circle can indeed be determined from the simulations by taking every possible pair of points on the circle $(\delta_i,\ \Delta_i)$ issued from the collisionality scan to compute a series of evaluations for $(C_\delta,\ R_\Delta)$:

$$C_\delta^{i\neq j} = \frac{\Delta_j^2 - \Delta_i^2 + \delta_j^2 - \delta_i^2}{2\left(\delta_j - \delta_i\right)} \tag{57}$$

$$R_\Delta^{i\neq j} = \left(\Delta_i^2 + (\delta_i - C_\delta^{i\neq j})^2\right)^{1/2} \tag{58}$$

and by taking the averaged values $\left\langle C_\delta^{i\neq j}\right\rangle$, $\left\langle R_\Delta^{i\neq j}\right\rangle$, and the standard deviations for estimating the error bars. Note that in contrast with the analytical model, this procedure does not assume that the circle intersects the origin. The collisional angle can be computed from the measured asymmetry and compared with the theoretical prediction. This is shown (for W^{44+}) in the right part of the two figures 13 and 14. A satisfactory agreement is found, although for the flat density case the determination of the center is rather imprecise outside $\sqrt{\psi} = 0.5$. The points of the collisionality scan indeed depart from the theoretical circle that intersects the origin since they give $\left\langle C_\delta^{i\neq j}\right\rangle > \left\langle R_\Delta^{i\neq j}\right\rangle$

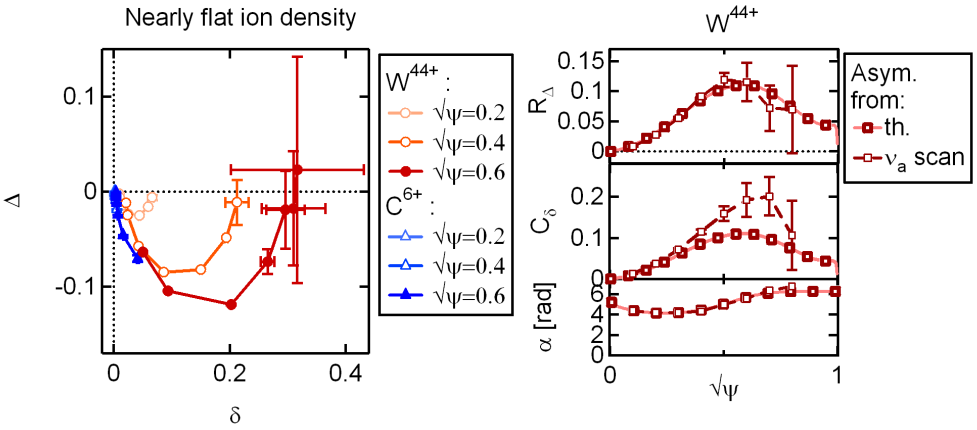

Figure 14. Trajectories of the W^{44+} and C^{6+} poloidal asymmetries at $\sqrt{\psi} = 0.2$, 0.4 and 0.6 (left), and comparison of the theoretical radius, center and collisional angle for W^{44+} at $\alpha_\nu = 1$ with its geometric determination during the collisionality scan (right), for the nearly flat ion density profile. The error bars correspond to the standard deviation of the evaluations made using equations (57) and (58).

in this spatial region. This discrepancy comes from the high collisionality points, where the horizontal asymmetry is found to be larger than the theoretical one, although the predicted flux remains close to the measured one (see figure 8).

4.4. Long term evolution

The impurity transport on the long term is expected to evolve to a situation without poloidal asymmetries, as shown in section 2.3. In order to test this analytical result, we have performed longer simulations for the peaked and nearly flat ion density profile cases, without artificial amplification of the impurity collision frequency ($\alpha_\nu = 1$).

We are interested in the slow evolution of the impurity density and its poloidal asymmetry, but there is first an initial phase where the impurity density organize itself to match the force balance that is assumed in the analytical theory. Since we start from a fully constant density, the asymmetry rapidly evolves by spiraling in the (δ, Δ) plane until this equilibrium is met, as shown in figure 15 for the flat ion density profile case (each point corresponds to an output of the simulation). The oscillations correspond to the eigenmode of the impurity evolution equation (44), with angular frequency ω and radial wave vector k that are solution of the (simplified) dispersion relation

$$\frac{\omega}{k} = -D_{PS}\frac{Z_a}{Z_i}\left[\partial_r \ln n_i - (C_0^a - 1)\partial_r \ln T_i)\right] \qquad (59)$$

The duration of this transitory phase increases with the radius considered. Because of the large excursion of the poloidal asymmetry in this phase, we had to increase the turbulent impurity transport diffusion coefficient at the very edge for the flat ion density case in the period $t \in [8,\ 53]$ ms, in order to avoid the formation of negative Tungsten density areas. We used a maximum value $D_\perp^{edge} = 0.16\, m^2/s$ in the period

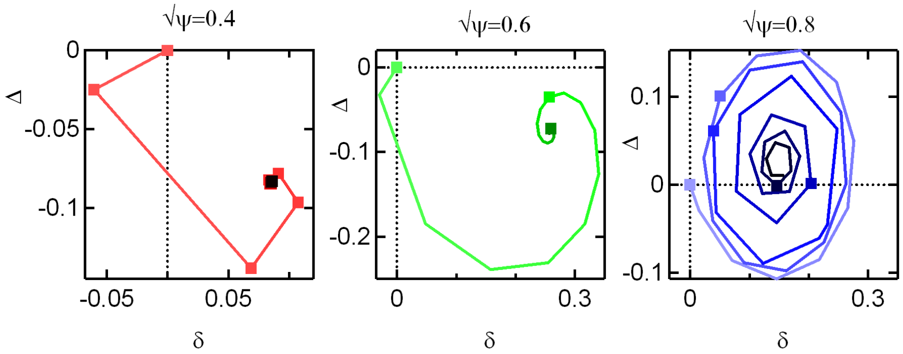

Figure 15. Transitory phase for the nearly flat ion density profile: (δ, Δ) evolution of W^{44+} at $\sqrt{\psi} = 0.4$ ($t < 10$ms), $\sqrt{\psi} = 0.6$ ($t < 10$ms) and $\sqrt{\psi} = 0.8$ ($t < 20$ms).

$t \in [8,\ 14]$ ms, $D_{\perp}^{edge} = 0.08\, m^2/s$ in the period $t \in [14,\ 43]$ ms, and $D_{\perp}^{edge} = 0.04\, m^2/s$ in the period $t \in [43,\ 53]$ ms, all being below D_{PS}^{edge}, as shown in figure 6. The amplitude of this edge turbulent diffusion was decreased slowly, but the oscillations in the (δ, Δ) plane were already stabilized within 20% of their equilibrium value after 30ms at $\sqrt{\psi} = 0.8$. The impact of this transitory modification of the edge impurity transport on the results that will be presented is presumably insignificant, because of its low amplitude, edge localization, and short application (see the description of figure 17). For our investigation on the long term evolution of the poloidal asymmetry, related with the evolution of the impurity profile and not with the establishment of the initial force balance, we need therefore to consider times typically larger than $t = 10$ms after the simulation starts, for radial positions inside $\sqrt{\psi} = 0.6$, so that the asymmetry parameters will be plotted only after this time in the coming figures. After this equilibration time, that applies to both the peaked and the flat ion density cases, the evolution of the poloidal asymmetry can be compared with the prediction of the analytical model, following the procedure explained in section 2.3. The simulations have been run for about 400ms, which is long enough to compare the asymmetry evolution with the theoretical predictions, but we are still far from the steady state equilibrium. The reason for this reduced time window comes from the computation time that is required, given the fact that the time step does not exceed few Alfvén times, i.e. about 1μs.

The evolution of the Carbon C^{6+} and Tungsten W^{44+} poloidal asymmetry, after the equilibration of the asymmetry parameters mentioned above, is shown in figure 16 for the peaked ion density profile. The figure includes the theoretical prediction using the procedure described in section 2.3 (dashed lines), and the prediction taking into account the actual asymmetries of the ion density and electrostatic potential (dotted lines). For Carbon, the trajectory in the (δ, Δ) plane is largely influenced by these asymmetries. In particular, the horizontal asymmetry is initially comparable in amplitude with the vertical one, whereas it would have been much lower with a poloidally

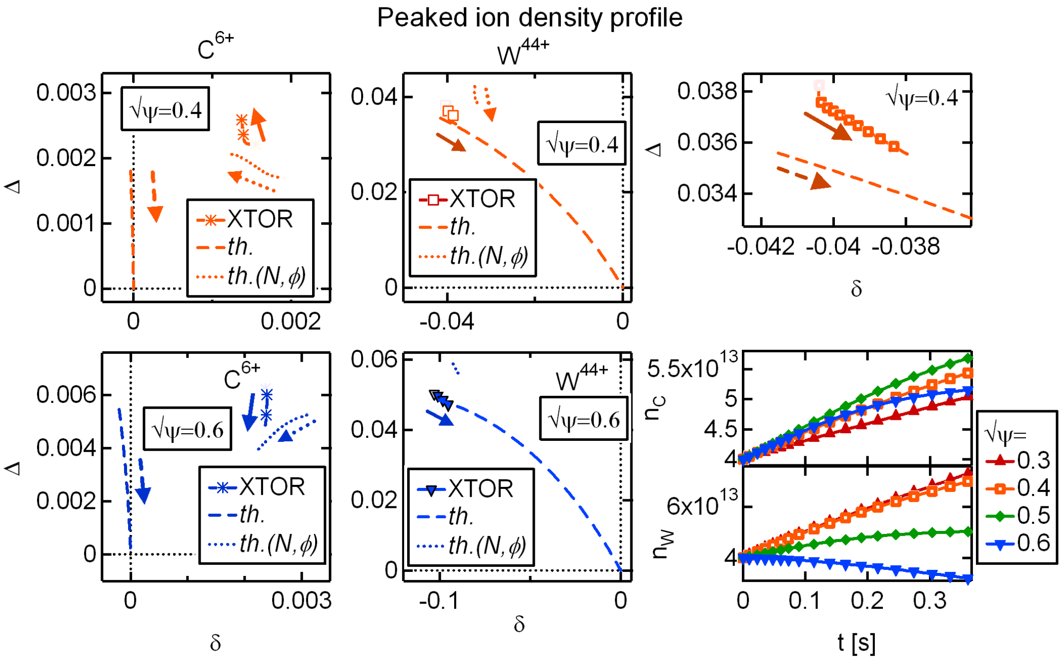

Figure 16. Trajectories in the (δ, Δ) plane for C^{6+} (left) and W^{44+} (middle) at $\sqrt{\psi} = 0.4$ (top)and $\sqrt{\psi} = 0.6$ (bottom) for the peaked ion density profile. Predictions from the analytical model are shown with a dashed line for $(\delta_\phi, \Delta_\phi) = (0\,0)$, and with a dotted line when using the measured value of $(\delta_\phi, \Delta_\phi)$ and (δ_N, Δ_N) . Right plots : zoom on the W^{44+} trajectory at $\sqrt{\psi} = 0.4$ (top) and evolution of the Carbon (middle) and Tungsten (bottom) concentrations. Arrows indicate the time evolution.

symmetric ion density and electrostatic potential. For Tungsten, the prediction without the asymmetries of the ion density and electrostatic potential is actually better than the more complete one, which overestimates the vertical asymmetry. But the predicted trajectories are in both cases consistent with the measured one, and they are directed towards a vanishing poloidal asymmetry.

The Tungsten and Carbon densities rise progressively in the plasma core, leading to a deleterious accumulation. In about 400 ms, the core Tungsten density has nearly doubled. However, only a small part of the trajectory in the (δ, Δ) plane has been completed in this period of time.

The same analysis is shown for the nearly flat ion density profile in figure 17. The initial asymmetry has a positive δ and negative Δ in this case, and Tungsten and Carbon concentrations become hollow thanks to the thermal screening. The analytical model predicts again a decrease of the asymmetry towards zero when the ion density and electrostatic potential are poloidally symmetric. For Carbon, the influence of the ion density and electrostatic potential asymmetries is also instrumental in determining the trajectory in the (δ, Δ) plane and the agreement with the theory prediction is nearly perfect in this case. But the trajectory is also deformed by the contribution of the main ion and electrostatic potential asymmetries for Tungsten. Regarding the impact of the transitory modification of the edge turbulent transport in the period $t \in [8,\ 53]$ms, it can be noted that this period ends when the vertical asymmetry at $\sqrt{\psi} = 0.4$ goes above -0.08 (top right plot of figure 17), that is to say very early in the trajectory that is simulated.

In these simulations, we observe that the evolution of the asymmetry is slow compared to that of the impurity concentration, in particular in the case of impurity accumulation (peaked ion density profile). Therefore, even if the trajectory towards a vanishing asymmetry is reproduced, the hypothesis of a trace impurity might be invalidated before the asymmetry has changed significantly. The final Tungsten peaking can be evaluated from the condition $\mathcal{G} = 0$ and it gives for the peaked ion density case $n_W(0)/n_W(0.5) \approx 70$ or $n_W(0)/n_W(0.6) \approx 5.6 \times 10^3$. The slow progress in the asymmetry evolution reflects therefore the large gap that remains to be covered after 400 ms before the steady state is reached. With such final value of the impurity peaking, the impact of the impurity accumulation is evidently huge. Then, core radiation will increase and impact both the electron and ion temperature, the safety factor profile, turbulent transport (including that affecting the impurity profile that is not taken into consideration here) and ion density. The situation of a stationary impurity profile without poloidal asymmetry is therefore impossible to reach in this case. Note that for the flat ion density case, the predicted steady state profile is on the opposite extremely hollow, with $n_W(0)/n_W(1) \approx 2 \times 10^{-10}$. These large equilibrium gradients result from the hypothesis of a highly charged Tungsten ion, which would not be the case in reality even if the transport was purely neoclassical, since the charge varies with temperature and would be low when approaching the plasma edge.

5. Conclusion

We have focused our work on the impurity transport and its relation to poloidal asymmetry in the absence of centrifugal force and temperature anisotropy. An analytical model, derived in the limit of a plasma configuration with circular cross section, shows that the vertical and horizontal asymmetries are positioned on a circle, characterized by a radius and center that depend on the density and temperature gradients, and an angle that depends on the collisionality. From this analytical model, we arrive to the conclusion that the steady state impurity profile has no poloidal asymmetries in the conditions mentioned above. When the electrostatic potential and main ion density are not poloidally symmetric, we find that the asymmetry of the impurity is still distributed on a circle, but its steady state value is no longer zero. This model has been tested with the MHD code XTOR where neoclassical physics and impurity evolution are implemented. The collision frequency between the impurity and the main ion species can be amplified so as to verify the main characteristics of the analytical model. We find a good agreement with theory predictions in the plasma core, with a discrepancy that increases towards the plasma edge where the analytical model becomes too simplified. The circle that links horizontal and vertical asymmetries is well reproduced in the simulations, as well as its collisional angle. Taking into account the asymmetry of

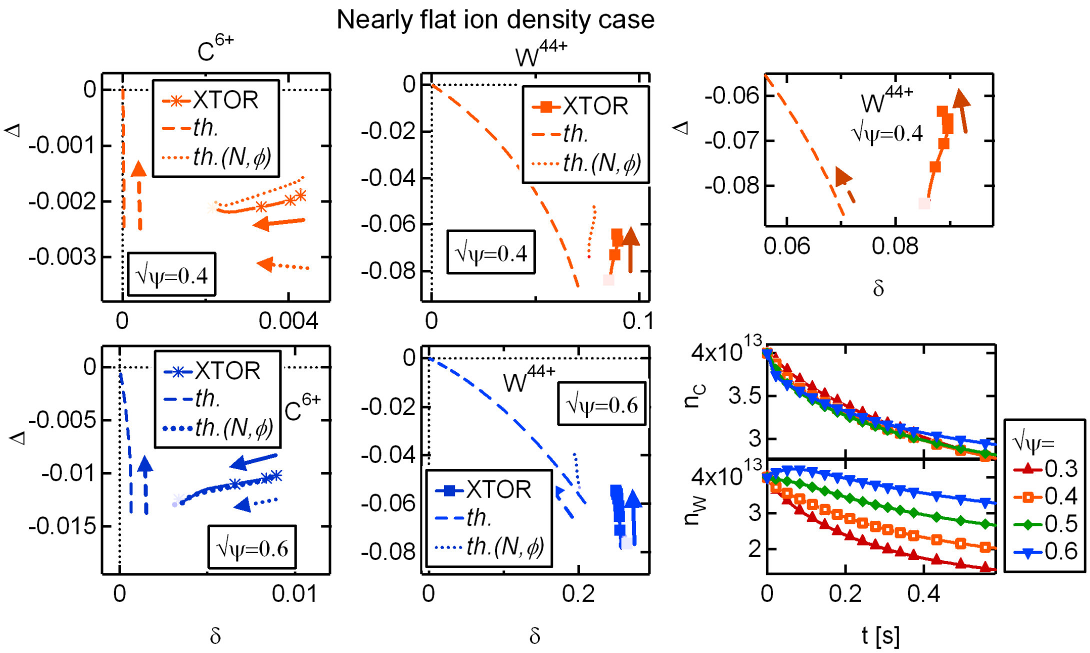

Figure 17. Trajectories in the (δ, Δ) plane for C^{6+} (left) and W^{44+} (middle) at $\sqrt{\psi} = 0.4$ (top)and $\sqrt{\psi} = 0.6$ (bottom) for the nearly flat ion density profile. Predictions from the analytical model are shown with a dashed line for $(\delta_\phi, \Delta_\phi) = (00)$, and with a dotted line when using the measured value of $(\delta_\phi, \Delta_\phi)$ and (δ_N, Δ_N) . Right plots : zoom on the W^{44+} trajectory at $\sqrt{\psi} = 0.4$ (top) and evolution of the Carbon (middle) and Tungsten (bottom) concentrations. Arrows indicate the time evolution.

the electrostatic potential in the theoretical prediction improves the agreement with the simulation results. To leading order, the long term evolution of the impurity distribution is found to be directed towards a vanishing asymmetry and therefore a steady state impurity profile that follows the simplest neoclassical prediction. However, the trajectory of the asymmetry is deformed by the contribution of the electrostatic potential and this effect is recovered in the simulations. The reduction of the asymmetry as the impurity profile evolves is representative of the distance between the actual state and the steady state without poloidal anisotropy. It can be, therefore, very slow, and in the case of impurity accumulation, the consequence of the increased core radiation and fuel dilution on the plasma scenario will be strong before the asymmetry has vanished. In this respect, the neoclassical impurity accumulation may lead to the activation of other mechanisms (core radiation, turbulence and the associated equilibrium change) before reaching a steady state, and the vanishing asymmetry can possibly never be reached.

An outcome of the analytical model is that, in principle, the impurity gradient could be derived from the measure of the poloidal asymmetry in plasmas verifying the hypotheses of the model, that is to say a low turbulent transport. In practice, this measurement is of course extremely delicate given the required precision on the equilibrium reconstruction and impurity concentration. But identification of poloidal asymmetries with error bars lower than 5% have already been reported, and they are easier to determine than the impurity concentration itself [18]. The contribution of turbulent transport in the evolution of impurities is however essential in most experimental situations [7, 33], except maybe in the very core of the plasma [34, 35] or when turbulent transport is largely suppressed in a transport barrier [36, 37, 38]. The analytical model could therefore be applicable in such conditions.

Another consequence relates to numerical simulations of impurity transport in conjunction with MHD. Indeed, unlike plasma resistivity that can be set to a larger value to accelerate the dynamics of MHD modes, neoclassical impurity transport cannot be artificially accelerated by increasing, for example, the collision frequency with the main ion species. This would increase the asymmetry angle and completely change the impurity dynamics, leading in general to a much weaker radial flux in the case of highly charged ions like Tungsten. For light impurities like Carbon, the situation is less critical and the collision frequency can be amplified significantly before the radial flux departs from a linear scaling. This issue is of particular concern when dealing with periodic MHD activity like sawteeth or ELMs whose relaxation period is fundamentally dependent on the resistive time scale. For the study of neoclassical impurity transport in the vicinity of a saturated island, this limitation does not apply.

Acknowledgments

This work has been carried out within the framework of the French Research Federation for Fusion Studies, and of the EUROfusion Consortium. It has received funding from the Euratom research and training programme 2014-2018 and 2019-2020 under grant agreement No 633053 for the project ENR-MFE19.CEA-03. We benefited from HPC resources from GENCI (project 056348), from Marconi-Fusion (project NISMO) and from Aix-Marseille Université project Equip@Meso (ANR-10-EQPX-29-01) of the program "Investissements d'Avenir" supervised by the Agence Nationale pour la Recherche. The authors thank the referees for their suggestions to improve the original manuscript. The views and opinions expressed herein do not necessarily reflect those of the European Commission.

References

[1] C. Angioni and A. G. Peeters. Direction of impurity pinch and auxiliary heating in tokamak plasmas. *Phys. Rev. Lett.*, 96:095003, Mar 2006.

[2] N. Dubuit, X. Garbet, T. Parisot, R. Guirlet, and C. Bourdelle. Fluid simulations of turbulent impurity transport. *Physics of Plasmas*, 14(4):042301, 2007.

[3] T. Fülöp, S. Braun, and I. Pusztai. Impurity transport driven by ion temperature gradient turbulence in tokamak plasmas. *Physics of Plasmas*, 17(6):062501, 2010.

[4] S. Futatani, X. Garbet, S. Benkadda, and N. Dubuit. Reversal of impurity pinch velocity in tokamaks plasma with a reversed magnetic shear configuration. *Phys. Rev. Lett.*, 104:015003, Jan 2010.

[5] G. R. McKee, M. Murakami, J. A. Boedo, N. H. Brooks, K. H. Burrell, D. R. Ernst, R. J. Fonck, G. L. Jackson, M. Jakubowski, R. J. La Haye, A. M. Messiaen, J. Ongena, C. L. Rettig, B. W. Rice, C. Rost, G. M. Staebler, R. D. Sydora, D. M. Thomas, B. Unterberg, M. R. Wade, and W. P. West. Impurity-induced turbulence suppression and reduced transport in the DIII-D tokamak. *Physics of Plasmas*, 7(5):1870–1877, 2000.

[6] R Guirlet, C Giroud, T Parisot, M E Puiatti, C Bourdelle, L Carraro, N Dubuit, X Garbet, and P R Thomas. Parametric dependences of impurity transport in tokamaks. *Plasma Physics and Controlled Fusion*, 48(12B):B63–B74, nov 2006.

[7] T Parisot, R Guirlet, C Bourdelle, X Garbet, N Dubuit, F Imbeaux, and P R Thomas. Experimental impurity transport and theoretical interpretation in a Tore Supra lower-hybrid heated plasma. *Plasma Physics and Controlled Fusion*, 50(5):055010, apr 2008.

[8] D. Villegas, R. Guirlet, C. Bourdelle, G. T. Hoang, X. Garbet, and R. Sabot. Experimental electron temperature gradient dependence of heavy impurity transport in fusion devices. *Phys. Rev. Lett.*, 105:035002, Jul 2010.

[9] N.T. Howard, M. Greenwald, D.R. Mikkelsen, M.L. Reinke, A.E. White, D. Ernst, Y. Podpaly, and J. Candy. Quantitative comparison of experimental impurity transport with nonlinear gyrokinetic simulation in an Alcator C-Mod L-mode plasma. *Nuclear Fusion*, 52(6):063002, apr 2012.

[10] C. Angioni, M. Sertoli, R. Bilato, V. Bobkov, A. Loarte, R. Ochoukov, T. Odstrcil, T. Pütterich, and J. Stober and. A comparison of the impact of central ECRH and central ICRH on the tungsten behaviour in ASDEX Upgrade H-mode plasmas. *Nuclear Fusion*, 57(5):056015, mar 2017.

[11] M. Sertoli, C. Angioni, and T. Odstrcil. Parametric dependencies of the experimental tungsten transport coefficients in ICRH and ECRH assisted ASDEX Upgrade H-modes. *Physics of Plasmas*, 24(11):112503, 2017.

[12] C Angioni and P Helander. Neoclassical transport of heavy impurities with poloidally asymmetric density distribution in tokamaks. *Plasma Physics and Controlled Fusion*, 56(12):124001, 2014.

[13] J.A Wesson. Poloidal distribution of impurities in a rotating tokamak plasma. *Nuclear Fusion*, 37(5):577–581, may 1997.

[14] M Romanelli and M Ottaviani. Effects of density asymmetries on heavy impurity transport in a rotating tokamak plasma. *Plasma Physics and Controlled Fusion*, 40(10):1767–1773, oct 1998.

[15] T. Fülöp and P. Helander. Nonlinear neoclassical transport in a rotating impure plasma with large gradients. *Physics of Plasmas*, 6(8):3066–3075, 1999.

[16] Ye O Kazakov, I Pusztai, T Fülp, and T Johnson. Poloidal asymmetries due to ion cyclotron resonance heating. *Plasma Physics and Controlled Fusion*, 54(10):105010, aug 2012.

[17] R. Bilato, O. Maj, and C. Angioni. Modelling the influence of temperature anisotropies on poloidal asymmetries of density in the core of rotating plasmas. *Nuclear Fusion*, 54(7):072003, apr 2014.

[18] M L Reinke, I H Hutchinson, J E Rice, N T Howard, A Bader, S Wukitch, Y Lin, D C Pace, A Hubbard, J W Hughes, and Y Podpaly. Poloidal variation of high-Zimpurity density due to hydrogen minority ion cyclotron resonance heating on Alcator C-Mod. *Plasma Physics and Controlled Fusion*, 54(4):045004, mar 2012.

[19] F J Casson, C Angioni, E A Belli, R Bilato, P Mantica, T Odstrcil, T Pütterich, M Valisa, L Garzotti, C Giroud, J Hobirk, C F Maggi, J Mlynar, and M L Reinke. Theoretical description of heavy impurity transport and its application to the modelling of tungsten in JET and ASDEX upgrade. *Plasma Physics and Controlled Fusion*, 57(1):014031, nov 2015.

[20] Hinrich Lütjens and Jean-François Luciani. XTOR-2F: A fully implicit Newton-Krylov solver applied to nonlinear 3D extended MHD in tokamaks. *Journal of Computational Physics*, 229(21):8130 – 8143, 2010.

[21] Patrick Maget, Olivier Février, Xavier Garbet, Hinrich Lütjens, Jean-Francois Luciani, and Alain Marx. Extended magneto-hydro-dynamic model for neoclassical tearing mode computations. *Nuclear Fusion*, 56(8):086004, 2016.

[22] T. Nicolas, H. Lütjens, J.-F. Luciani, X. Garbet, and R. Sabot. Impurity behavior during sawtooth activity in tokamak plasmas. *Physics of Plasmas*, 21(1):012507, 2014.

[23] Jae-H Ahn, X Garbet, H Lütjens, and R Guirlet. Dynamics of heavy impurities in non-linear MHD simulations of sawtoothing tokamak plasmas. *Plasma Physics and Controlled Fusion*, 58(12):125009, 2016.

[24] S.P. Hirshman and D.J. Sigmar. Neoclassical transport of impurities in tokamak plasmas. *Nuclear Fusion*, 21(9):1079–1201, sep 1981.

[25] Patrick Maget, Olivier Février, Xavier Garbet, Hinrich Lütjens, Jean-Francois Luciani, and Alain Marx. Corrigendum: Extended magneto-hydro-dynamic model for neoclassical tearing mode computations (2016 nucl. fusion 56 086004). *Nuclear Fusion*, 59(4):049501, mar 2019.

[26] H. Lütjens, A. Bondeson, and O. Sauter. The CHEASE code for toroidal MHD equilibria. *Computer Physics Communications*, 97(3):219–260, 1996.

[27] T. Hirai, H. Maier, M. Rubel, Ph. Mertens, R. Neu, E. Gauthier, J. Likonen, C. Lungu, G. Maddaluno, G.F. Matthews, R. Mitteau, O. Neubauer, G. Piazza, V.Philipps, B. Riccardi, C. Ruset, and I. Uytdenhouwen. R&D on full tungsten divertor and beryllium wall for JET ITER-like wall project. *Fusion Engineering and Design*, 82(15):1839 – 1845, 2007. Proceedings of the 24th Symposium on Fusion Technology.

[28] K. Krieger, H. Maier, and R. Neu. Conclusions about the use of tungsten in the divertor of ASDEX Upgrade. *Journal of Nuclear Materials*, 266-269:207 – 216, 1999.

[29] D M Yao, G N Luo, Z B Zhou, L Cao, Q Li, W J Wang, L Li, S G Qin, Y L Shi, G H Liu, and J G Li. Design, r&d and commissioning of EAST tungsten divertor. *Physica Scripta*, T167:014003, dec 2015.

[30] J. Bucalossi, A. Argouarch, V. Basiuk, O. Baulaigue, P. Bayetti, M. Bcoulet, B. Bertrand, S. Brémond, P. Cara, M. Chantant, Y. Corre, X. Courtois, L. Doceul, A. Ekedahl, F. Faisse, M. Firdaouss, J. Garcia, L. Gargiulo, C. Gil, C. Grisolia, J. Gunn, S. Hacquin, P. Hertout, G. Huysmans, F. Imbeaux, G. Jiolat, M. Joanny, L. Jourdheuil, M. Jouve, A. Kukushkin, M. Lipa, S. Lisgo, T. Loarer, P. Maget, R. Magne, Y. Marandet, A. Martinez, D. Mazon, O. Meyer, M. Missirlian, P. Monier-Garbet, P. Moreau, E. Nardon, S. Panayotis, B. Pégourié, R.A. Pitts, C. Portafaix, M. Richou, R. Sabot, A. Saille, F. Saint-Laurent, F. Samaille, A. Simonin, and E. Tsitrone. Feasibility study of an actively cooled tungsten divertor in Tore Supra for ITER technology testing. *Fusion Engineering and Design*, 86(6-8):684 – 688, 2011. Proceedings of the 26th Symposium of Fusion Technology (SOFT-26).

[31] R A Pitts, A Kukushkin, A Loarte, A Martin, M Merola, C E Kessel, V Komarov, and M Shimada. Status and physics basis of the ITER divertor. *Physica Scripta*, T138:014001, dec 2009.

[32] C.E. Kessel. Bootstrap current in a tokamak. *Nucl. Fusion*, 34(9):1221–1238, 1994.

[33] M. Valisa, L. Carraro, I. Predebon, M.E. Puiatti, C. Angioni, I. Coffey, C. Giroud, L. Lauro Taroni, B. Alper, M. Baruzzo, P. Belo daSilva, P. Buratti, L. Garzotti, D. Van Eester, E. Lerche, P. Mantica, V. Naulin, T. Tala, and M. Tsalas and. Metal impurity transport control in JET H-mode plasmas with central ion cyclotron radiofrequency power injection. *Nuclear Fusion*, 51(3):033002, feb 2011.

[34] R. Dux, A.G. Peeters, A. Gude, A. Kallenbach, R. Neu, and ASDEX Upgrade Team. Z dependence of the core impurity transport in ASDEX Upgrade H mode discharges. *Nuclear Fusion*, 39(11):1509, 1999.

[35] R Dux, R Neu, A G Peeters, G Pereverzev, A M ck, F Ryter, J Stober, and ASDEX Upgrade Team. Influence of the heating profile on impurity transport in ASDEX upgrade. *Plasma Physics and Controlled Fusion*, 45(9):1815–1825, aug 2003.

[36] P.C Efthimion, S. Von Goeler, W.A Houlberg, E.J Synakowski, M.C Zarnstorff, S.H Batha, R.E Bell, M Bitter, C.E Bush, F.M Levinton, E Mazzucato, D.C McCune, D Mueller, H.K Park, A.T Ramsey, A.L Roquemore, and G Taylor. Observation of neoclassical transport in reverse shear plasmas on TFTR. *Nuclear Fusion*, 39(11Y):1905–1909, nov 1999.

[37] T. Sunn Pedersen, R.S Granetz, A.E Hubbard, I.H Hutchinson, E.S Marmar, J.E Rice, and J Terry.

Radial impurity transport in the H mode transport barrier region in Alcator C-Mod. *Nuclear Fusion*, 40(10):1795–1804, oct 2000.

[38] T. Pütterich, R. Dux, M.A. Janzer, and R.M. McDermott. ELM flushing and impurity transport in the H-mode edge barrier in ASDEX Upgrade. *Journal of Nuclear Materials*, 415(1, Supplement):S334 – S339, 2011. Proceedings of the 19th International Conference on Plasma-Surface Interactions in Controlled Fusion.

[39] K.W. Wenzel and D.J. Sigmar. Neoclassical analysis of impurity transport following transition to improved particle confinement. *Nuclear Fusion*, 30(6):1117–1127, jun 1990.

Appendix A. Impurity flux without asymmetry in the ion density

We consider in this work an axisymmetric equilibrium and we express the magnetic field as $\mathbf{B} = F\nabla\varphi + \nabla\varphi \times \nabla\psi$ with a Jacobian $J^{-1} = \nabla\psi \cdot \nabla\theta \times \nabla\varphi$. The steady state momentum equation of a species 'a' of fluid velocity $\mathbf{V_a}$ writes:

$$-\nabla p_a + n_a e_a \left(\mathbf{E} + \mathbf{V_a} \times \mathbf{B}\right) + \mathbf{R_a} = 0 \tag{A.1}$$

where $\mathbf{R_a}$ is the friction force (we neglect here the pressure anisotropy, see section Appendix B).

The scalar product of equation (A.1) with $R^2\nabla\varphi$ gives the radial particle flux:

$$\Gamma_a \cdot \nabla\psi = \; - n_a \mathbf{E} \cdot R^2\nabla\varphi - \frac{\mathbf{R_a}}{e_a} \cdot R^2\nabla\varphi \tag{A.2}$$

Using the relation :

$$R^2\nabla\varphi = \frac{F}{B^2}\mathbf{B} - \frac{\mathbf{B} \times \nabla\psi}{B^2} \tag{A.3}$$

we obtain:

$$\Gamma_a \cdot \nabla\psi = \; - n_a \frac{F}{B^2}\left(\mathbf{E}\cdot\mathbf{B} + \frac{\mathbf{R_a}\cdot\mathbf{B}}{e_a n_a}\right) + n_a \mathbf{E} \cdot \frac{\mathbf{B} \times \nabla\psi}{B^2} + \frac{\mathbf{R_a}}{e_a} \cdot \frac{\mathbf{B} \times \nabla\psi}{B^2} \tag{A.4}$$

where we have, using $\mathbf{E} \equiv -\nabla\phi$:

$$\mathbf{E} \cdot \frac{\mathbf{B} \times \nabla\psi}{B^2} = \left(1 - \frac{F^2}{R^2B^2}\right)\partial_\varphi\phi - \frac{F}{JB^2}\partial_\theta\phi \tag{A.5}$$

The projection parallel to $\mathbf{B}$ of equation (A.1) gives, using $J \equiv 1/\mathbf{B}\cdot\nabla\theta$:

$$\mathbf{E}\cdot\mathbf{B} + \frac{\mathbf{R_a}\cdot\mathbf{B}}{e_a n_a} = \frac{1}{J}\frac{\partial_\theta p_a}{e_a n_a} \tag{A.6}$$

which, injected into equation (A.4) gives:

$$\begin{aligned} \Gamma_a \cdot \nabla\psi = \; & - \frac{F}{e_a J B^2}\left(\partial_\theta p_a + e_a n_a \partial_\theta\phi\right) \\ & + \frac{\mathbf{R_a}}{e_a} \cdot \frac{\mathbf{B} \times \nabla\psi}{B^2} + n_a\left(1 - \frac{F^2}{R^2B^2}\right)\partial_\varphi\phi \end{aligned} \tag{A.7}$$

We neglect in the following the third term that corresponds to the classical flux [39], as well as the inductive field component (last term).

From equation (A.6) we get:

$$R_{a\parallel} = \frac{n_a T_a}{JB}\left[\frac{\partial_\theta p_a}{n_a T_a} + \frac{e_a}{T_a}\partial_\theta\phi\right] \tag{A.8}$$

so that equation (A.7) becomes:

$$\Gamma_a \cdot \nabla\psi \approx -\frac{F}{e_a B} R_{a\|} \tag{A.9}$$

The parallel friction can be expressed as (see Appendix B):

$$R_{a\|} = -n_a m_a \nu_a \left(V_{a\|} - V_{i\|} + C_0^a \frac{2q_{i\|}}{5p_i} \right) \tag{A.10}$$

$$C_0^a = \frac{3}{2} \frac{1}{1 + \frac{T_a}{T_i}\frac{m_i}{m_a}} \tag{A.11}$$

where C_0^a comes from equation (B.6). We need therefore to express the parallel flows in order to compute the impurity flux.

The assumption of stationarity $\nabla \cdot (n_a \mathbf{V_a}) = 0$ gives

$$\frac{1}{J}\partial_\psi \left(J n_a \mathbf{V_a} \cdot \nabla\psi\right) + \frac{1}{J}\partial_\theta \left(J n_a \mathbf{V_a} \cdot \nabla\theta\right) + \frac{1}{J}\partial_\varphi \left(J n_a \mathbf{V_a} \cdot \nabla\varphi\right) = 0 \tag{A.12}$$

We assume that the first term is negligible, which to leading order means that the radial flux is constant in the radial direction. This assumption is reasonable when considering smooth plasma profiles, but can easily break when the second derivative of the profiles becomes large, e.g. in the vicinity of a transport barrier or of a magnetic island. In the axisymmetric case ($\partial_\varphi = 0$) we then have :

$$\frac{\mathbf{V_a} \cdot \nabla\theta}{\mathbf{B} \cdot \nabla\theta} = \frac{K_a(\psi)}{n_a} \tag{A.13}$$

where $K_a(\psi)$ is an unknown function.

From equation (A.1), the fluid velocity can be expressed as:

$$\mathbf{V_a} = \frac{V_{a\|}}{B}\mathbf{B} + \frac{T_a}{e_a} A_a \frac{\mathbf{B} \times \nabla\psi}{B^2} + \frac{T_a}{e_a} A_a^\theta \frac{\mathbf{B} \times \nabla\theta}{B^2} \tag{A.14}$$

where $A_a = \partial_\psi \ln p_a + (e_a/T_a)\partial_\psi \phi$ and $A_a^\theta = \partial_\theta \ln p_a + (e_a/T_a)\partial_\theta \phi$. From this expression we obtain

$$\frac{\mathbf{V_a} \cdot \nabla\theta}{\mathbf{B} \cdot \nabla\theta} = \frac{V_{a\|}}{B} + \frac{F}{B^2}\frac{T_a}{e_a} A_a \tag{A.15}$$

This gives using equation (A.13):

$$V_{a\|} = \frac{K_a(\psi)}{n_a} B - \frac{T_a}{e_a} A_a \frac{F}{B} \tag{A.16}$$

Similarly for $q_{i\|}$, using $\nabla \cdot \mathbf{q_i} = 0$ and $q_{i\perp} = \frac{5}{2} p_i \mathbf{V^*_{Ti}}$ with $\mathbf{V^*_{Ti}} = \left(\mathbf{B} \times \nabla T_i\right)/(e_i B^2)$, we can write:

$$q_{i\|} = L_i(\psi) B - \frac{5}{2}\frac{p_i}{e_i}\frac{F}{B}\partial_\psi T_i \tag{A.17}$$

These equations express the parallel velocity and fluxes as a function of the thermodynamic forces A_s and a constant, yet to be determined. It is possible to eliminate these constants by carrying appropriate flux surface averages, as shown below.

Using the notations $u_{2\|i} = 2q_{i\|}B/(5p_i)$ and $N = n_i/\langle n_i \rangle$ we can write:

$$\begin{aligned} u_{2\|i} &= \frac{2L_i(\psi)}{5\langle n_i \rangle T_i}\frac{B^2}{N} - F\frac{\partial_\psi T_i}{e_i} \\ &= \langle u_{2\|i} \rangle \frac{B^2/N}{\langle B^2/N \rangle} + \left(\frac{B^2/N}{\langle B^2/N \rangle} - 1\right) F\frac{\partial_\psi T_i}{e_i} \end{aligned} \qquad \text{(A.18)}$$

We define :

$$u(\psi) = \frac{K_i(\psi)}{\langle n_i \rangle} - \frac{C_0^a}{\langle B^2/N \rangle}\left(F\frac{\partial_\psi T_i}{e_i} + \langle u_{2\|i} \rangle\right) \qquad \text{(A.19)}$$

At equilibrium, since the surface average cancels the operator $(\mathbf{B}\cdot\nabla)$, the parallel projection of equation (A.1) gives (assuming isothermal flux surfaces):

$$T_a \left\langle B\nabla_\| \ln n_a \right\rangle + e_a \left\langle B\nabla_\| \phi \right\rangle = 0 \qquad \text{(A.20)}$$

so that $\left\langle BR_{a\|}/n_a \right\rangle = 0$, and using equation (A.10) we obtain:

$$K_a \left\langle \frac{B^2}{n_a} \right\rangle - K_i \left\langle \frac{B^2}{n_i} \right\rangle + C_0^a \langle u_{2\|i} \rangle - F\frac{T_a}{e_a}A_a + F\frac{T_i}{e_i}A_i = 0 \qquad \text{(A.21)}$$

This gives, using equations (A.19) and (A.21) to eliminate K_i and K_a:

$$\begin{aligned} \frac{R_{a\|}}{n_a m_a \nu_a} &= \frac{F}{B}\left(\frac{T_a}{e_a}A_a - \frac{T_i}{e_i}A_i + C_0^a\frac{\partial_\psi T_i}{e_i}\right)\left(1 - \frac{B^2/n_a}{\langle B^2/n_a \rangle}\right) \\ &\quad + \frac{u(\psi)}{B}\left\langle \frac{B^2}{N} \right\rangle \left(\frac{B^2/N}{\langle B^2/N \rangle} - \frac{B^2/n_a}{\langle B^2/n_a \rangle}\right) \end{aligned} \qquad \text{(A.22)}$$

The radial flux then writes:

$$\begin{aligned} \langle \Gamma_a \cdot \nabla\psi \rangle &= m_a \nu_a \frac{F^2 T_a}{e_a^2}\left[\left(\frac{1}{\left\langle \frac{B^2}{n_a} \right\rangle} - \left\langle \frac{n_a}{B^2} \right\rangle\right)\left(\partial_\psi \ln p_a - \frac{T_i}{T_a}\frac{e_a}{e_i}\partial_\psi \ln p_i + C_0^a\frac{e_a}{e_i}\frac{\partial_\psi T_i}{T_a}\right)\right. \\ &\quad \left. + \frac{u(\psi)}{F}\frac{e_a}{T_a}\left(\frac{\langle B^2/N \rangle}{\langle B^2/n_a \rangle} - \langle n_a/N \rangle\right)\right] \end{aligned} \qquad \text{(A.23)}$$

In presence of neoclassical friction, one can expect the poloidal ion flow to follow its neoclassical drive, i.e. [21]:

$$\left[\mathbf{V_i} + k_i\left(\mathbf{V^*_{Ti}} + \frac{u_{2\|i}}{B^2}\mathbf{B}\right)\right]\cdot\nabla\theta \approx 0 \qquad \text{(A.24)}$$

We have:

$$\left[\mathbf{V_i} + k_i\left(\mathbf{V^*_{Ti}} + \frac{u_{2\|i}}{B^2}\mathbf{B}\right)\right]\cdot\nabla\theta = \frac{\mathbf{B}\cdot\nabla\theta}{N}\left[\frac{K_i(\psi)}{\langle n_i \rangle} + \frac{k_i}{\langle B^2/N \rangle}\left(F\frac{\partial_\psi T_i}{e_i} + \langle u_{2\|i} \rangle\right)\right] \qquad \text{(A.25)}$$

and equation (A.19) becomes therefore:

$$u(\psi) = -\frac{C_0^a + k_i}{\langle B^2/N \rangle}\left(F\frac{\partial_\psi T_i}{e_i} + \langle u_{2\|i} \rangle\right) \qquad \text{(A.26)}$$

Equation (A.22) can then be expressed as:

$$\frac{R_{a\parallel}}{n_a m_a \nu_a} = \frac{F}{B}\left(\frac{T_a}{e_a}A_a - \frac{T_i}{e_i}A_i + C_0^a\frac{\partial_\psi T_i}{e_i}\right)\left(1 - \frac{B^2/n_a}{\langle B^2/n_a\rangle}\right)$$
$$- \left(C_0^a + k_i\right)\frac{F}{B}\left(\frac{\partial_\psi T_i}{e_i} + \frac{\left\langle u_{2\parallel i}\right\rangle}{B}\right)\left(\frac{B^2/N}{\langle B^2/N\rangle} - \frac{B^2/n_a}{\langle B^2/n_a\rangle}\right) \tag{A.27}$$

and the radial flux becomes:

$$\langle \Gamma_a \cdot \nabla\psi\rangle = m_a\nu_a\frac{F^2 T_a}{e_a^2}\left[\left(\frac{1}{\left\langle\frac{B^2}{n_a}\right\rangle} - \left\langle\frac{n_a}{B^2}\right\rangle\right)\left(\partial_\psi \ln p_a - \frac{T_i}{T_a}\frac{e_a}{e_i}\partial_\psi \ln p_i + C_0^a\frac{e_a}{e_i}\frac{\partial_\psi T_i}{T_a}\right)\right.$$
$$\left. + \left(C_0^a + k_i\right)\frac{e_a}{T_a}\left(\frac{\partial_\psi T_i}{e_i} + \frac{\left\langle u_{2\parallel i}\right\rangle}{B}\right)\left(\frac{\langle n_a/N\rangle}{\langle B^2/N\rangle} - \frac{1}{\langle B^2/n_a\rangle}\right)\right] \tag{A.28}$$

The poloidal asymmetry can be obtained from equation (A.8) assuming isothermal flux surfaces:

$$\partial_\theta \ln n_a + \frac{e_a}{T_a}\partial_\theta\phi = JB\frac{R_{a\parallel}}{n_a T_a} \tag{A.29}$$

Appendix B. Coefficients for the impurity momentum equation

The parallel momentum equation for impurity species can be expressed in the same way as for the main ion. Using the same notations as in [21] but neglecting the collisions between the impurity and electrons, we have

$$m_a n_a D_t V_{a\parallel} = -\nabla_\parallel p_a + n_a e_a E_\parallel + R_{a\parallel} - \left(\nabla\cdot\Pi_a\right)_\parallel \tag{B.1}$$

$$\frac{R_{a\parallel} - \left(\nabla\cdot\Pi_a\right)_\parallel}{m_a n_a} = \Lambda_{11}^{ai}V_{i\parallel} + \Lambda_{11}^{aa}V_{a\parallel} + \Lambda_{12}^{ai}\frac{2q_{i\parallel}}{5p_i} + \Lambda_{12}^{aa}\frac{2q_{a\parallel}}{5p_a}$$
$$- \mu_1^a\left(V_{a\parallel} + S_1^a/B\right) - \mu_2^a\left(\frac{2q_{a\parallel}}{5p_a} + S_2^a/B\right) \tag{B.2}$$

with $D_t \equiv \partial_t + \left[\left(V_{\parallel a}\mathbf{b} + \mathbf{V_E}\right)\cdot\nabla V_{\parallel a}\mathbf{b}\right]\cdot\mathbf{b}$ and

$$\begin{pmatrix} S_1^a \\ S_2^a \end{pmatrix} = \frac{B^2}{\mathbf{B}\cdot\nabla\theta}\begin{pmatrix} \mathbf{V_a^*} + \mathbf{V_E} \\ \mathbf{V_{Ta}^*} \end{pmatrix}\cdot\nabla\theta \tag{B.3}$$

for all species 'a'. The notations are identical to that adopted in reference [21], and all neoclassical coefficients are computed following reference [32].

We assume that the parallel heat flux is at equilibrium, that impurity is trace, and that the interaction between the impurity and the electrons can be neglected. We can then express the mean parallel impurity heat flux as a function of the mean parallel flow in a similar ways as it was done for parallel heat flows of ions and electrons in [21, 25]:

$$\left\langle\frac{2q_{a\parallel}B}{5p_a}\right\rangle = C_\parallel^{aa}\left\langle \mathbf{V_a}\cdot\mathbf{B}\right\rangle + C_\parallel^{ai}\left\langle \mathbf{V_i}\cdot\mathbf{B}\right\rangle + C_{\parallel,2}^{ai}\left\langle\frac{2q_{i\parallel}B}{5p_i}\right\rangle + C_1^a\left\langle S_1^a\right\rangle + C_2^a\left\langle S_2^a\right\rangle \tag{B.4}$$

with:

$$\nu_a \;= \Lambda_{11}^{ai} = -\Lambda_{11}^{aa} \tag{B.5}$$

$$C_0^a \;= \;-\Lambda_{12}^{ai}/\Lambda_{11}^{ai} = \frac{3}{2}\frac{1}{1+\frac{T_a}{T_i}\frac{m_i}{m_a}} \tag{B.6}$$

$$C_\parallel^{aa} \;= \;-\frac{\Lambda_{21}^{aa}-\mu_2^a}{\Lambda_{22}^{aa}-\mu_3^a}, \qquad C_\parallel^{ai} = -\frac{\Lambda_{21}^{ai}}{\Lambda_{22}^{aa}-\mu_3^a} \tag{B.7}$$

$$C_{\parallel,2}^{ai} = \;-\frac{\Lambda_{22}^{ai}}{\Lambda_{22}^{aa}-\mu_3^a}, \qquad C_1^a = \frac{\mu_2^a}{\Lambda_{22}^{aa}-\mu_3^a} \tag{B.8}$$

$$C_2^a \;= \frac{\mu_3^a}{\Lambda_{22}^{aa}-\mu_3^a}, \qquad C_q^a = \Lambda_{12}^{aa}-\mu_2^a \tag{B.9}$$

so that

$$\frac{R_{a\parallel}-(\nabla\cdot\Pi_a)_\parallel}{m_a n_a} = \nu_a\left(V_{i\parallel}-V_{a\parallel}-C_0^a\frac{2q_{i\parallel}}{5p_i}\right)+C_q^a\frac{2q_{a\parallel}}{5p_a}-\mu_1^a\left(V_{a\parallel}+\frac{S_1^a}{B}\right)-\mu_2^a\frac{S_2^a}{B} \tag{B.10}$$

For all species ”s”’ we have

$$\frac{2q_{s\parallel}B}{5p_s} = \left\langle\frac{2q_{s\parallel}B}{5p_s}\right\rangle\frac{B^2}{\langle B^2\rangle}+\left(\frac{B^2}{\langle B^2\rangle}-1\right)S_2^s \tag{B.11}$$

The coefficient ν_a is normalized to the Alfvén time, and it can be multiplied by a free factor α_ν. This rescaling is also automatically applied to C_q^a and $\mu_{1,2}^a$.

In the neoclassical parallel friction force described in equation (B.10), the three last terms are in general negligible. The neoclassical friction coefficients $\mu_{\cdots}^a$ are small compared with the $\Lambda_{\cdots}^{ai}$ coefficients, and we have:

$$C_q^a/(C_0^a\nu_a) \approx \Lambda_{12}^{aa}/\Lambda_{12}^{ai} \approx m_i/m_a \tag{B.12}$$

This explains why a simplified momentum equation like (A.6) is generally sufficient to describe heavy impurity transport in tokamaks.